An Integrated Graphene-MXene Electrochemical Transistor Array Platform for Accurate Prostate Cancer Diagnosis Using Plasma sEV-Derived E2F5 Biomarker

Piyali Mukherjee(0000-0002-1583-5831), Nahid Sultana, Grutanjali Sahu, Isha Goyal, Laxmidhar Besra, Pritam Das, Debansu Sarkar, Debasree Bishnu, Pooja Sharma, Sanghamitra Sengupta(0000-0002-1752-6143), Sriparna Chatterjee*(0000-0002-3161-1010), Chirasree RoyChaudhuri*(0000-0001-9619-4150)*

Piyali Mukherjee, Chirasree RoyChaudhuri
Department of Electronics & Telecommunication Engineering, Indian Institute of Engineering Science and Technology, Shibpur, Howrah-711103, West Bengal, India
E-mail: chirashree@telecom.iiests.ac.in

Grutanjali Sahu, Laxmidhar Besra, Sriparna Chatterjee
Materials Chemistry & Interfacial Engineering Department, CSIR-Institute of Minerals and Materials Technology, Bhubaneswar-751013, Odisha, India
E-mail: sriparna251@gmail.com

Nahid Sultana, Sanghamitra Sengupta
Department of Biochemistry, University of Calcutta, 35, Ballygunge Circular Road, Kolkata-700019, West Bengal, India.
Pritam Das
School of Advanced Material Engineering, Kookmin University, Seongbok-gu, Seoul 02707, Republic of Korea.
Debansu Sarkar
Department of Urology, IPGMER and SSKM Hospital, 244, A.J.C. Bose Road, Kolkata-700020, West Bengal, India.
Debasree Bishnu
Department of Cell Biology, John C Martin Centre for Liver Research and Innovations, 33A, Jawaharlal Nehru Rd, Park Street area, Kolkata-700071, West Bengal, India.
Isha Goyal, Pooja Sharma
Material Science and Sensor Applications, CSIR-Central Scientific Instruments Organization, Sector-30, Chandigarh, Punjab, India.

Keywords: Graphene-Mxene, transistor, E2F5 marker, exosomes, prostate cancer, benign.

Exosomes have been investigated for diagnosis of prostate cancer (PC) due to their capability of offering real-time reflection of tumor burden. However, discriminating benign prostatic hyperplasia (BPH) from healthy controls (HC) and varying PC grades remains a challenge in clinical settings. Here, an ultrasensitive electrochemical field-effect transistor based on porous graphene-MXene composites has been constructed that circumvents the Debye screening limitations in detecting large biomolecular targets like exosomes. Additionally, the device leverages synergistic interfacial effects to enhance receptor binding density which contributes to high sensitivity leading to a detection limit of 200 exosomes/ml (approximately three orders of magnitude lower than the most sensitive antibody-based reports), with a wide range (~10^8 exosomes/ml) and detection time within 30 minutes. Further, dielectrophoresis (DEP) enabled in-situ exosome enrichment is integrated enabling direct analysis of clinical samples without ultracentrifugation. Most importantly, the efficacy of E2F5 as exosomal protein has been validated for accurate PC diagnosis in all patient cohorts. Multiple features have been extracted from sensor response and analyzed using ensemble classification method. Interestingly, the outcomes reveal that the sensor successfully distinguished BPH from HCs with appreciable accuracy of 91.11% and shows similar diagnostic performance with lower grade PC, higher grade PC and healthy patients.

1. Introduction

Prostate cancer (PC) is the second most commonly diagnosed cancer worldwide and the fifth leading cause of cancer-related mortality among men.[1] Diagnosis typically involves digital clinical examination including rectal examination (DRE), serum prostate-specific antigen (PSA) test and transrectal ultrasound (TRUS)-guided biopsy. Various risk stratification systems incorporating pathological factors such as Gleason score, PSA levels, and clinical and pathological staging have been established. Unfortunately, these methods fail to reliably differentiate between indolent and aggressive prostate cancer at the time of detection, often leading to over-diagnosis and overtreatment.[2] Further, Benign prostatic hyperplasia (BPH) and prostate cancer exhibit distinct cellular growth patterns and arise from different regions of the prostate gland, they often coexist and share overlapping symptoms and risk factors.[3] The limited specificity of PSA testing to differentiate BPH and prostate cancer often results in unnecessary biopsies and associated morbidities in the diagnosis of BPH. Consequently, there

is an urgent need for the development of a minimally invasive diagnostic tool capable of accurately distinguishing between BPH and prostate cancer.

Traditional surgical biopsies, even when supplemented with genomic information, provide only a limited snapshot of an ongoing dynamic process. Liquid biopsies present an alternative approach for efficient disease monitoring and follow-up. Circulating extracellular vesicles (EV) serve as a valuable source of cancer-derived molecules in liquid biopsies, offering a real-time reflection of tumor burden. In the context of prostate cancer, multiple studies have investigated exosomes or small EVs (sEV) based diagnostic strategies, highlighting their promises. Recent research has established E2F5, a dual-function transcription factor, which is consistently upregulated in prostate cancer tissues and subsequently deregulates TGF-β/p38/SMAD3 signalling axis drives uncontrolled cell proliferation.[4] E2F5 suppresses the transcription of TFPI-2 while promoting the expression of MMP2 and MMP9. The E2F5-mediated loss of TFPI-2 activity plays a central role in cancer cell aggressiveness, epithelial-mesenchymal transition (EMT), and metastasis.[5,6] A semi-quantitative assessment of protein abundance using the Western blot technique in plasma-sEV suggests that E2F5 could be a promising biomarker for diagnosing clinically significant prostate cancer and monitoring disease progression.[7] However, the efficacy of this biomarker for accurate prostate cancer diagnosis in clinical settings has not been investigated.

In this context, various sensing strategies have been widely explored for sEV detection in multiple cancers.[8,9] Moreover, microfluidics enabled efficient exosome enrichment platforms with fast and simple operation for pre-concentration has gained significant attention. In this aspect, few recent endeavors propose construction of a 3D porous sponge microfluidic chip and aptamer functionalized magnetic Ti_3C_2 composite material[10,11], resulting in differentiation of early stage cancer from normal patients. However, these pre-concentration methods are coupled with sophisticated fluorescence measurements to enable low detection limits. Contemporary reviews on exosome detection encompassing the various electrical biosensing methodologies reveal that electrochemical transistors (FET) have the potential to reach lower detection limits without any labels or complex surface modification strategies deploying simple instrumentation[12,13].

In this context, graphene field effect transistors have been the most investigated due to its stability towards environmental parameters in comparison to the transition-metal dichalcogenides.[14] However, these sensors, even with decorated nanoparticles fail to detect below 10^5 particles ml^{-1} which may be caused by screening of the charges of exosomes by the Debye layer even at lower molar strengths of 1 mM buffer due to larger size in the range of 30

nm to 200 nm.[15-17] Diverse efforts have been undertaken by facilitating advanced measurement scheme and functional materials such as heterodyne detection[18], molecular imprinted polymers[19], deformable aptamers[20], wrinkled graphene and surface engineering by nanopore formation[21]. Although these approaches resulted in augmented sensitivity of FETs in ionic solutions, most of them have certain limitations. Aptamers have the capability of altering their conformation upon binding with target molecules thereby leading to an enhanced signal [22-23] but their clinical translation is often affected by the time consuming and labor-intensive SELEX technology-based design [24]. The heterodyne detection, results in complexity of the operating circuitry. Another inspiring approach to overcome Debye length limitations involves development of crumpled or wrinkled graphene structures in GFETs but the fabrication processes either introduce defects or are not reliable, especially when crumpling dimensions need to match the size of exosomes which are typically greater than 50 nm. Synthesizing molecularly imprinted polymers will not be a practical approach for exosome detection due to the heterogeneity in the dimension of the latter across different categories of patients. In this aspect pore formation on graphene can be most appropriate in extending the Debye volume. Further, it is desirable to enhance the receptor binding sites on graphene for sensitivity enhancement. Various top down and bottom up approaches have been documented to generate pores on graphene[25-27]. Physical etching by ion or electron beam can yield uniform pores of varying dimensions but the high cost associated with the complicated setups coupled with the physical damage imparted to the material limit their widespread applications. Traditional bottom up methods following organic synthesis and template directed approach can result in ordered and adjustable pore morphology but their complex preparation steps and critical template removal process hinders large scale development. In-plane pore construction techniques based on directional recombination have been reported to address the above disadvantages. However, although the performance of porous graphene with larger surface area and edge active sites have been demonstrated to exhibit efficient solute molecule/ion transport and more solid electrolyte interface as battery electrodes, it still falls short of meeting the requirement of high receptor binding sites for ultrasensitive biosensing applications. Thus, an alternate scalable strategy of introducing new materials for pore formation can allow for integration of different functional groups through synergistic effects, which may expand the sensing performance of porous graphene composites. In this direction, it has been recently reported that graphene integrated with MXene layers (a class of two-dimensional (2D) materials composed of transition metal carbides, nitrides, or carbonitrides with a general formula $M_{n+1}X_nT_x$, where M stands for a transition metal, X stands for either carbon and/or nitrogen,

and T_x represents surface functional groups like -OH, -F, -O etc.[28,29]) enhances the bioreceptor binding through covalent bonding with the surface functional groups. Further MXene-doped semiconductors have been researched to have higher carrier density and hence increased transconductance[30]. In light of the above discussion, the development of graphene-MXene composites with a porous architecture, while preserving the semiconducting characteristics of reduced graphene oxide, a direction that remains largely unexplored, may represent a promising strategy to address the longstanding challenge of Debye shielding in electrochemical FETs. Pure MXene and graphene nanosheets tend to form a more stacked structure during drying due to the strong π–π interactions and van der Waals forces between the individual sheets. However, when mixed together, they are more likely to cross-link, leading to the formation of pores, which is likely a result of the repulsive interactions between the flakes. Additionally, there has been no dedicated effort of in-situ exosome pre-concentration in electrochemical field effect transistors. Most importantly, gradation of different tumor stages from benign to malignant by liquid biopsy approach remains an unresolved issue, specially by field deployable electrical methods.

This study presents a first-of-its-kind ultrasensitive electrochemical field-effect transistor based on a porous graphene-MXene composite architecture that preserves the semiconducting properties of reduced graphene oxide, thereby circumventing Debye screening limitations in the detection of large biomolecular target like exosomes. Further, the device, fabricated by scalable approach also enhances the receptor binding density through synergistic effects. Additionally, the manuscript introduces two underexplored advances. First, dielectrophoresis (DEP)-enabled in situ exosome enrichment is integrated to substantially enhance detection sensitivity, enabling direct exosome analysis from clinical samples without ultracentrifugation. Such approach has been minimally explored in FET-based exosome sensing. Second, the study establishes the clinical superiority of E2F5 over the conventional marker CD63 for exosome-based prostate cancer diagnostics, particularly in discriminating healthy and benign prostatic hyperplasia (BPH) cohorts. Sensor responses from anti-E2F5-functionalized devices, coupled with machine learning assisted classification, enable non-invasive, high-fidelity exosome sensing and robust stratification of patients into healthy, benign, and high-grade prostate cancer categories. The proposed sensing platform thereby has the potential for escalating the translation of electrochemical transistors into clinical practice.

2. Results and Discussions

2.1. Working principle of graphene-MXene electrochemical transistor

FETs developed through the integration of MXene with graphene are known to enhance bioreceptor binding via covalent interactions with surface functional groups[31]. These hybrid semiconductors also exhibit higher carrier density, resulting in improved transconductance[32]. MXene FET has been fabricated by depositing layered structures of MXene on graphene.[31] However, fabrication of graphene-MXene composite with porous morphology retaining the semiconducting behavior has not been explored as electrochemical transistors. The pore dimension has been tuned to match closely the diameter of exosomes. The charged exosomes trapped within the dense pores will have limited volume for ions to approach and generate significant screening effect. Hence, the field emanating from these exosomes within the pores persist farther away, thereby disrupting the conventional Debye layer formation. The Debye length which is the characteristic length of the diffuse double layer depends on the ionic strength of the solution. Exosomes after being captured within the pores can result in significant overlap of the double layers between the external surface of exosomes and internal surface of pores, thereby prohibitng complete shielding of the surface charge of exosomes. Further there is a possibility of long range ordering of water molecules and ion within the confined space of the pores which can also significantly reduce the ability of the ions to form gradients. This effect is represented in **Figure 1a**. Approximating the concave pore surfaces as spherical, the enhanced Debye length (λ′) can be estimated from equation 1[33]:

$$\lambda' = \lambda / \left(\coth(x) - \frac{1}{x} \right) \quad (1)$$

where *x* is a dimensionless radius variable given by $x = {}^{R}/_{\lambda}$, R is the effective radius of pores and λ is the Debye length. Considering the approximate diameter of the exosomes to be between 50-130 nm, as discussed in subsequent sections, the surface charges of these molecules outside the Debye layer are screened by a surrounding layer of ions; however, due to the comparable size of the pores and the enhanced penetration depth of the ionic screening layer, the latter originating from the exosome surface overlaps with that formed at the inner surface of the pores, thereby reducing the extent of charge screening.

The sensor with coplanar gate electrode is fabricated on a printed circuit board with the channel length and the distance between the drain and source electrodes and gate as 100 µm, which is limited by the resolution of the printing process (**Figure 1b**). The volume enclosed by the three electrodes of the transistor platform can contain 100 µl of the analyte (Device fabrication details in **Supporting Information S1**). As the height of the analyte is typically around 2 mm, diffusion mediated capture of exosomes not only limits the sensitivity but also

increases the detection time. To address these limitations, combining DEP and AC electroosmosis can enable selective and efficient particle concentration. The latter helps in driving them towards the sensor surface from the bulk liquid while the former preferentially pre-concentrates the exosomes at a selected frequency on the channel surface. Though electrochemical FET has been documented to differentiate between exosomes of normal patients and cancer patients of advanced grade, detection at early stage of malignancy and its distinction with benign tumour is challenging since the sensor electrical output overlaps to some extent for closely matched exosomes count and dimensions in the noisy plasma background. To enable this, multiple features have been extracted from the drain-source current measurements to develop an AI based ensemble classification system to discriminate PC patients from non-PC populations efficiently (**Figure 1c**).

2.2. Exosome characterization

For the isolation of small extracellular vesicles, 500 µl of plasma samples were subjected to a series of sequential centrifugation steps, as detailed in **Supporting Information S2**. Small EVs were isolated from plasma samples of four study groups, including prostate cancer patients categorized by low-grade (Gleason Score 7) and high-grade (Gleason Score 9) tumors, healthy controls, and individuals diagnosed with benign prostatic hyperplasia.

The physicochemical properties of the isolated sEVs, including size distribution and particle concentration, were characterized using dynamic light scattering (DLS), nanoparticle tracking analysis (NTA) and transmission electron microscopy (TEM). The number of patient samples from whom exosomes have been extracted is 20 for each group (healthy, BPH, PC7 and PC 9). To ensure reproducibility, each sample has been analyzed in five independent runs, resulting in 100 DLS measurements per group. The mean and standard deviation of the DLS results revealed statistically significant variation in sEV size across the groups (**Figure 2a**), increasing from healthy control to BPH and PCs. Particle concentration and size distribution were further analyzed using a NanoSight NS300 system (Malvern Panalytical) with NTA software version 3.0. For each sample, five independent measurements were recorded, with 30-60 second videos capturing particle trajectories. The NTA data revealed notable differences in particle size among the groups (**Figure 2b**), particularly highlighting the presence of smaller-sized sEVs in the healthy control group compared to the prostate cancer and BPH groups.

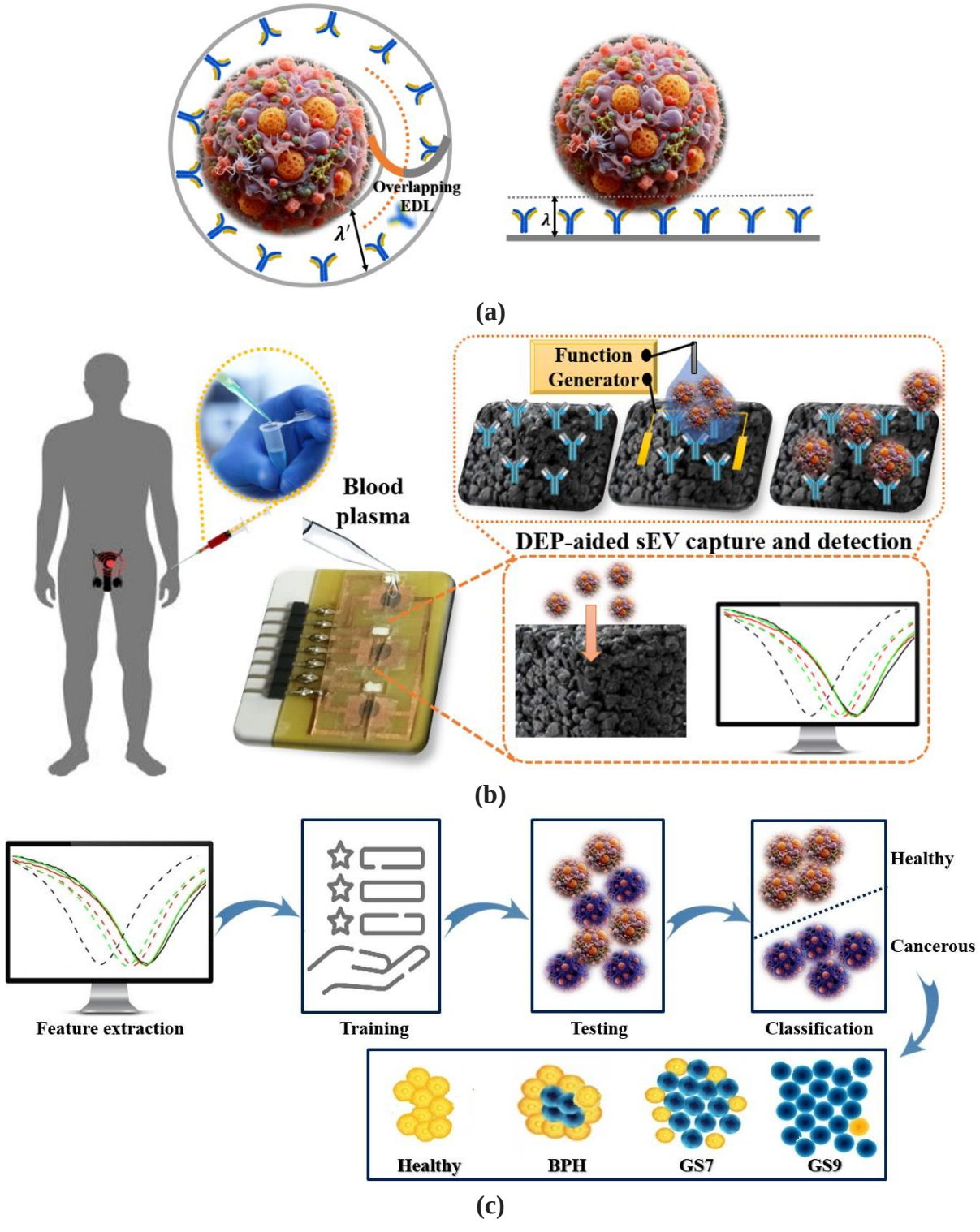

Figure 1. (a) Schematic illustration of the impact of Debye length modulation upon exosome capture within a nanopore versus a planar surface. On the left, an exosome captured within a nanopore functionalized with recognition probes leads to geometrical confinement, causing the EDLs originating from the pore walls and the exosome surface to overlap significantly. In contrast, the right panel depicts exosome binding on a flat functionalized surface, where the EDL develops from the planar interface, leading to weaker electrostatic modulation due to

efficient ionic screening in the bulk electrolyte. The comparison highlights the critical role of nanopore-induced EDL overlap in improving sensitivity for exosome detection. (b) Schematic overview of DEP-assisted small extracellular vesicle (sEV) capture and electrical detection from blood plasma using a functionalized FET biosensing platform. (c) Machine-learning assisted classification workflow for sEV-based disease stratification, illustrating the end-to-end data analytics pipeline applied to electrically measured sensor responses.

Morphological validation of the sEVs were performed using TEM. The samples were fixed with 2.5% glutaraldehyde, loaded onto epoxy resin, and negatively stained with uranyl acetate. Typical TEM image of exosomes extracted from BPH patient confirmed the presence of spherical EVs with characteristic lipid bilayers (**Figure 2c**), dimensions ranging from 50-120 nm, consistent with size distribution observed from DLS. **Figure 2d** summarizes the variation in sEV dimensions and concentration across different patient groups, estimated from NTA and DLS. To verify the prostate-specific origin and validate the expression of tumor-associated markers, Western blot (WB) analysis was conducted. The presence of CD9, CD63, and CD81, the canonical sEV markers, confirmed the successful isolation of sEVs. Furthermore, the detection of KLK3 (also known as PSA) validated their prostate-derived origin. Notably, E2F5, a transcription factor implicated in promoting prostate cancer cell proliferation and invasion, was abundantly detected in the sEVs, suggesting its potential role as a tumor-associated biomarker (**Figure 2e**). In addition, by quantifying exosomal E2F5 levels in plasma samples obtained from 20 healthy individuals, 20 BPH patients and 20 PC patients each with Gleason scores of 7 and 9 each, we observed a statistically significant elevation of exosomal E2F5 expression with increasing disease severity. In particular, E2F5 levels were markedly higher in GS7 and GS9 groups compared to healthy and BPH cohorts (***$p < 0.001$), underscoring the potential diagnostic and stratification capability of exosomal E2F5 in distinguishing malignant prostate cancer states from benign and healthy conditions (**Figure 2f**).

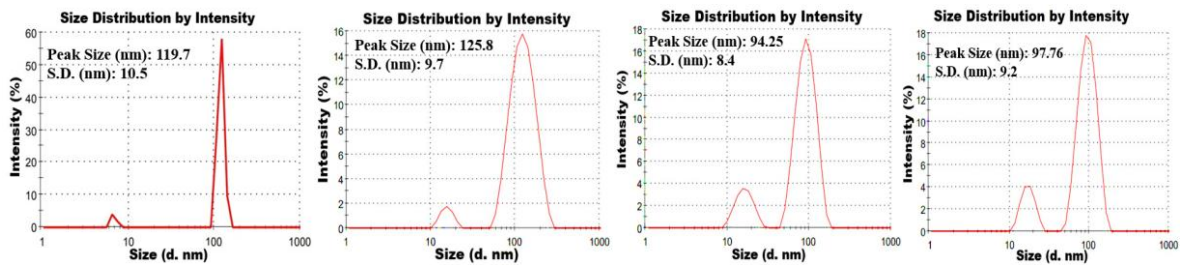

(a)

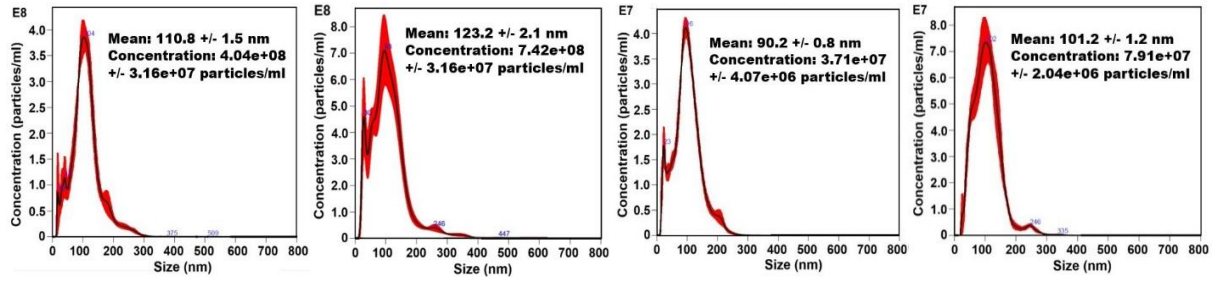

(b)

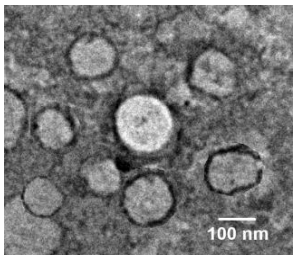

(c)

	Prostate Cancer with Gleason Score		Normal	BPH	p-value
	7 (3+4)	9 (4+5)			
EV characteristics					
Sample no. (N)	45	60	60	45	
Size by DLS (nm)	119.7 ± 10.50	125.8 ± 9.7	94.25 ± 8.4	97.76 ± 9.2	0.01
Size by NTA (nm)	110.8 ± 1.5	123.2 ± 2.1	90.2 ± 0.8	101.2 ± 1.2	0.001
Concentration by NTA (particles/ml)	$4.04 \times 10^8 \pm 3.16 \times 10^7$	$7.42 \times 10^8 \pm 3.16 \times 10^7$	$3.71 \times 10^7 \pm 4.07 \times 10^6$	$7.91 \times 10^7 \pm 2.04 \times 10^6$	0.01

(d)

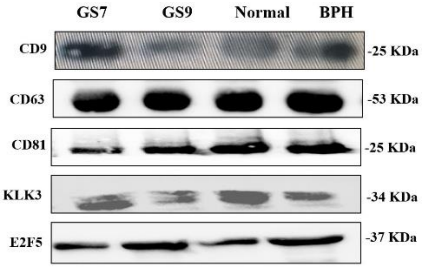

(e)

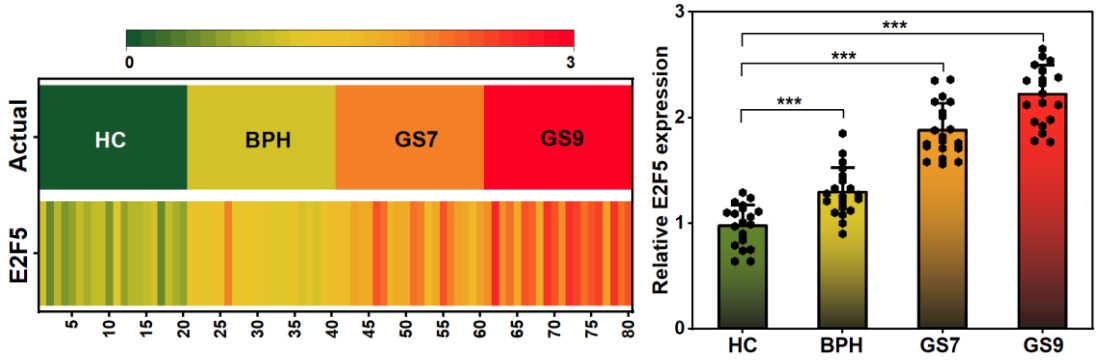

(f)

Figure 2. Comprehensive physicochemical and molecular characterization of small extracellular vesicles (sEVs) across different patient groups. (a) DLS analysis showing the hydrodynamic size distribution of sEVs, highlighting variations in mean diameter GS7, GS9, healthy and BPH from left to right), (b) NTA profiles for the four patient groups (GS7, GS9, healthy and BPH from left to right), providing quantitative information on particle size distribution and sEV concentration, (c) Representative TEM image of sEVs isolated from a BPH patient, confirming vesicular morphology. (d) Summary of sEV size and concentration across all patient groups, as extracted from DLS and NTA measurements, illustrating disease-dependent trends in vesicle dimensions and abundance, (e) Western blot analysis of sEV protein markers for all patient groups, enabling comparison of relative marker expression across disease states, (f) Quantification of E2F5 expression in plasma-derived exosomes from HCs (n = 20), BPH patients (n = 20), and PC patients of grade 7 and 9 (n = 41-80). ***$p < 0.001$.

2.3. Preparation and Characterization of the graphene-MXene films

The composite of graphene oxide (GO, Terracarb Pvt. Ltd.) and Mxene, GMX, has been prepared by mixing commercially available GO with synthesized few-layer MXene in an aqueous medium at varying weight ratios of 3:1, 1:1 and 1:3. Description of the fabrication process has been detailed in **Supporting Information S3a**. The composite solution has been then spin coated on the sensor substrate and thermally annealed at 300°C for 30 minutes to yield graphene (reduced graphene oxide)-MXene layer. The typical SEM images are represented in **Figure 3 (a-c).** It has been observed that a porous nanocomposite has been formed with pores varying from 50 nm to 150 nm approximately for GMX ratio varying from 3:1, 1:1 and 1:3 respectively. To quantitatively evaluate the influence of GMX weight ratios on the resulting porous architecture, SEM images obtained from GMX films prepared with different graphene-MXene mixing ratios were systematically analyzed using image analysis software. The average pore sizes were extracted under each condition to enable a comparative morphological assessment. Pure MXene and graphene nanosheets are known to form densely stacked lamellar structures during drying, driven primarily by strong π–π interactions and van der Waals forces between adjacent sheets. In contrast, when graphene and MXene are combined, the hetero-interactions between the two nanomaterials promote cross-linking and suppress excessive restacking, leading to the formation of interconnected pores. In particular, the mechanical flexibility of graphene sheets facilitates the development of a more open and porous network, while repulsive interactions between dissimilar flakes further enhance pore formation. From a biosensing perspective, the presence of such interconnected pores plays a crucial role in modulating the electrochemical environment at the sensor surface. Specifically, the porous GMX structure can impede the formation of a rigid electrical double layer (EDL) around captured targets, thereby mitigating Debye screening effects and enabling more effective charge transduction at the FET channel.

Recognizing that reproducibility in FET fabrication and uniformity in electrical response are critical prerequisites for clinical translation, reliability analysis has been performed across different chip sets. In addition, predefined exclusion criteria have been established prior to clinical testing (discussed in subsequent section) to further enhance data consistency and detection robustness. The FET biosensor platform has been developed on printed circuit boards (referred as chip sets) where each board comprises of 390 individual FET sensors, generating a total of 1170 individual sensors. Each GMX mixing ratio (3:1, 1:1 and 1:3) has been tested with 30 sensors selected from three chip sets. Each sensor has been imaged across ten different fields

and the average along with standard deviation has been computed across all the 30 sensors for every ratio. In **Figure 3d**, histograms represent the distribution of pore diameters across 30 sensors for each mixing ratio. The mean pore diameter for 3:1, 1:1 and 1:3 has been obtained to be around 70 nm, 100 nm and 130 nm respectively. The bar graphs in **Figure 3e** depict the statistical deviation among chips, providing a quantitative measure of chip-level variability. Both these collectively illustrate the impact of GMX composition on sensor reproducibility, a basic requirement for scalable and clinically relevant sensing. Further, specific surface area has been estimated from BET analysis. Each GMX ratio has been tested on five samples and f**igure 3(f-h)** presents the average nitrogen adsorption-desorption isotherms for GMX ratios of 3:1, 1:1 and 1:3 respectively. All three samples exhibit Type IV isotherms with hysteresis loops, confirming the mesoporous nature of the composites. The average specific surface area for all the composites have been tabulated in **Figure 3i.** The 3:1 and 1:1 GMX composites exhibit comparable specific surface area, confirming that a balanced graphene-MXene ratio or graphene rich composites effectively suppresses MXene restacking. In contrast, 1:3 GMX shows reduced surface area despite the presence of large voids observed in SEM, which can be attributed to dense lamellar stacking of MXene sheets. The average pore size distribution of all three GMX composites have been obtained from the Barrett-Joyner-Halenda (BJH) model. Porous nature of 3:1 GMX shifts toward smaller mesopores and partial micropores, while 1:1 GMX results in narrow, well-defined mesopore peak centered around 100 nm, while larger mesopore distribution has been obtained for 1:3 GMX ratio, all of which are consistent with the obtained porous morphology from SEM measurements. **Figure 3j** presents the XRD patterns of GMX composites with different graphene-MXene ratios. The 1:3 GMX sample displays a pronounced low-angle diffraction peak centered around $2\theta \approx 7°$, corresponding to the (002) plane of MXene. The sharpness of this peak indicate strong lamellar ordering and dense stacking of MXene sheets. Upon incorporation of rGO, the MXene (002) diffraction peak shifts to $2\theta \approx 4.5°$, indicating the coexistence of distinct interlayer spacing within the 1:1 GMX composite, while this peak slightly broadens for 3:1 GMX ratio. The increased interlayer distance may be attributed to the intercalation of graphene layers between adjacent MXene sheets.

The average FTIR spectra, conducted on five samples for each GMX ratio (**Figure 3k**) show presence of vibrational bands due to C=O, C=C, and C-O bonds, which are characteristics of graphene oxide. A small peak at 550 cm^{-1} may indicate presence of metal-oxygen bond which appears due to the presence of MXene in the system. The average Raman spectra, performed on five samples for each GMX ratio indicate presence of distinct peaks assigned to G band and

D band (**Figure 3l)** indicating the presence of carbon and disorder in the samples[34]. X-ray photoelectron spectroscopy (XPS) has also been performed for characterizing the chemical composition and state of the elements. At binding energies of around 285, 458, 530 and 680 eV, corresponding to C 1s, Ti 2p, O 1s, and F 1s, all GMX samples exhibit four distinctive peaks (**Figure 3m**). Additionally, noteworthy changes were observed in the fine structure of deconvoluted O 1s spectra shown in **Figure 3(n-p)**, indicating the presence of distinct changes in chemical environment associated with various oxygen species. Deconvolution of the broad O 1s spectra using Gaussian peak fitting reveals the appearance of three peaks centered at around 529.5 eV, 530.5 eV, and 532 eV, which may be attributed to the presence of Ti-O, C-Ti-O, and C-Ti-OH or C=O moiety. In addition, **Figure S1(a,b)** represents the deconvoluted spectrum of C 1s of the composites. The three subpeaks at 284.6 eV, 286.7 eV, and 288. 4 eV emerge from the C-C, C-O, and C-O=O moieties. In all these cases, the presence of a peak at 282 eV is observed which corresponds to Ti-C bonding. This confirms the formation of nanocomposite. The details of all the characterization methods are discussed in **Supporting Information S3b**.

Further, graphene-MXene interaction has been modeled using Vienna Ab initio Software Package (VASP) (details in **Supporting Information S3c**). To model the experimental MXene-graphene structure, aluminium has been first removed from the Ti_3AlC_2 structure. Subsequently, both the top and bottom Ti layers of the resulting Ti_3C_2 structure have been saturated with OH or F groups, and the structure has been fully optimized. The lattice vectors in the XY plane have been adjusted for the relaxed supercells, while the Z-direction parameter has been fixed at 20 Å to prevent interactions between periodic images (**Supporting Figure S2a** and **Table S1**). Three different structures have been considered with reduced graphene oxide (rGO):MXene weight ratios of 3:1, 1:1, and 1:3, in accordance with experiments. **Figure 3(q-s)** illustrates the optimized electrode structure of OH-terminated MXene with rGO at these weight ratios. The OH-terminated MXene structure migrates toward rGO, forming hydrogen bonds between the two materials. However, the interlayer distance within the MXene structure remains unchanged. The optimized structure of F-terminated MXene with rGO at different weight ratios (**Supporting Figure S2b**) reveals similar findings as OH-terminated MXene, with no appreciable difference between the interaction energies.

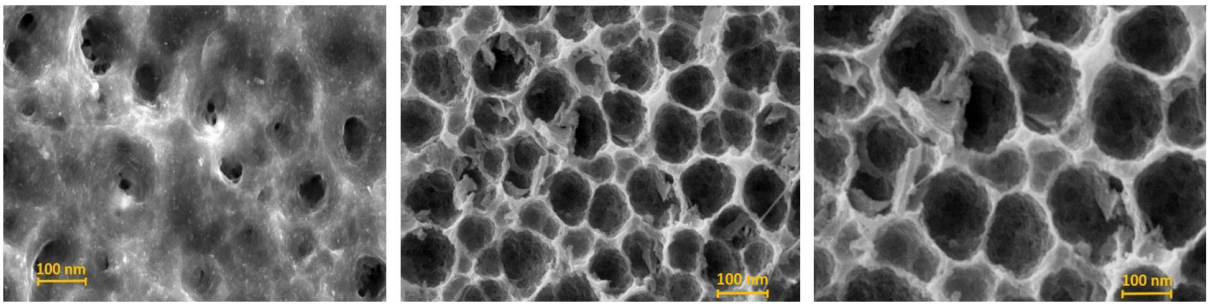

(a) (b) (c)

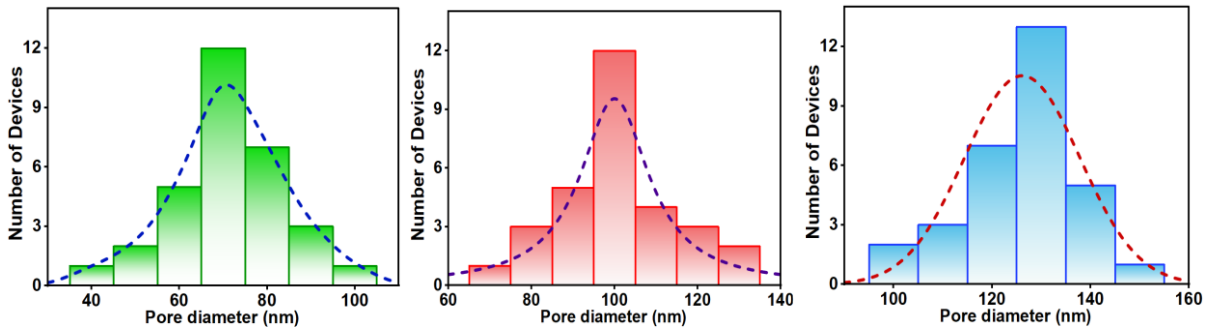

(d)

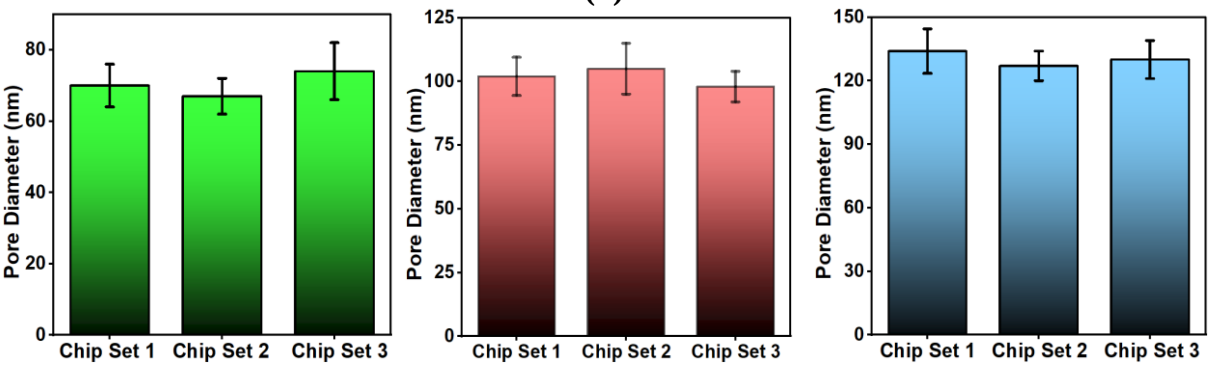

(e)

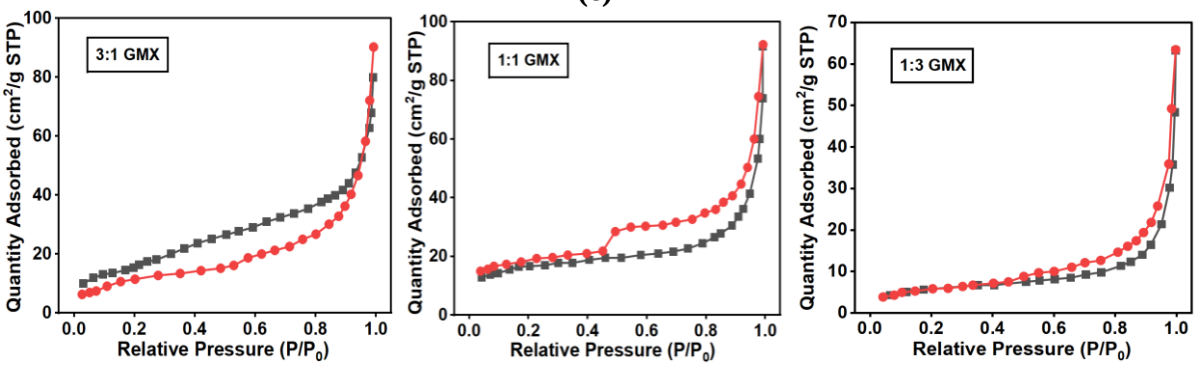

(f) (g) (h)

GMX Ratio	BET SSA ($m^2 g^{-1}$)	Avg. BJH Pore Diameter (nm)
3:1	75.1	78
1:1	69.6	102
1:3	45.5	124

(i)

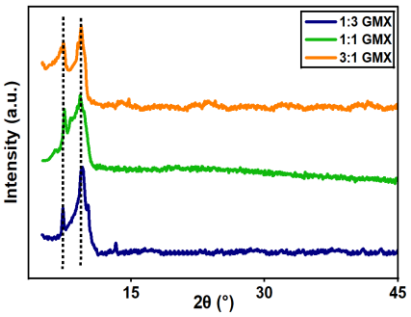

(j)

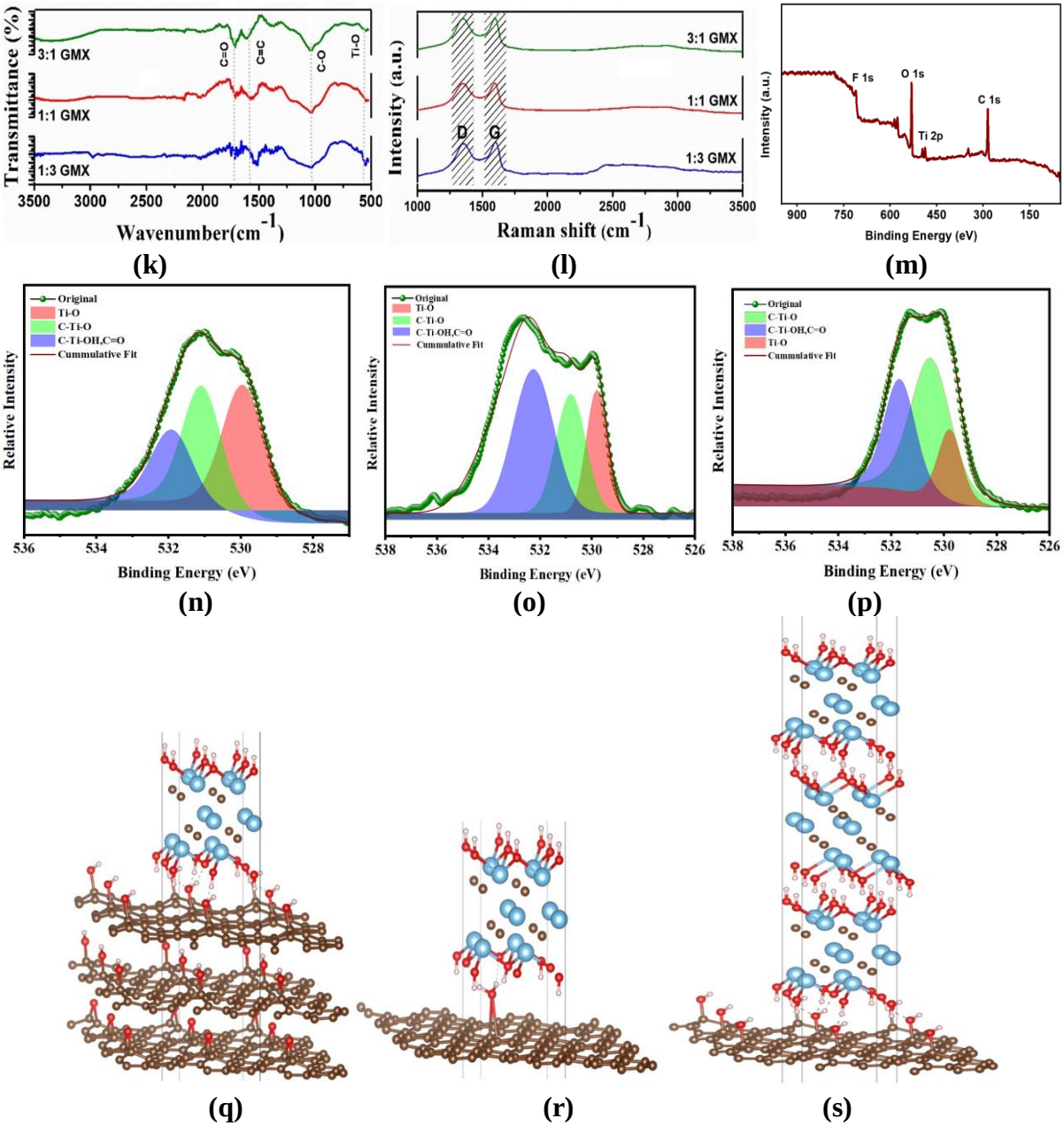

Figure 3. (a-c) SEM images of graphene-MXene nanocomposites prepared at GMX weight ratios of 3:1, 1:1 and 1:3, respectively, illustrating the evolution of porous morphology with composition. (d) Histograms showing the distribution of pore diameters across 30 sensors for each GMX composition, highlighting intra-chip uniformity; the mean pore diameters for 3:1, 1:1, and 1:3 ratios are approximately 70 nm, 100 nm and 130 nm, respectively. (e) Bar graphs depicting chip-to-chip statistical deviations of 30 sensors for each GMX ratio, providing a quantitative assessment of device reproducibility. (f-h) Average Nitrogen adsorption/desorption isotherms of 3:1, 1:1 and 1:3 GMX composites. (i) The average specific surface area and average pore diameter obtained from BET for the three composites. (j) XRD patterns of GMX composites with different graphene-MXene ratios. (k) FTIR spectra and (l) Raman spectra of the GMX nanocomposites (obtained as average of 5 sensors for each ratio), confirming

successful hybridization and interfacial interactions between graphene and Mxene. (m) XPS spectra of 1:1 GMX. (n-p) XPS analysis of GO-MXene nanocomposites, O 1s spectra of 1:3, 1:1 and 3:1 GMX respectively, (q-s) Optimized electrode structures of rGO integrated with OH-terminated MXene at weight ratios of 1:3, 1:1, and 3:1, respectively, obtained from structural modelling; blue, red, brown, white and gray spheres represent Ti, O, C, H, and F atoms, respectively.

2.4. Antibody immobilization on graphene-MXene composite

In the antibody immobilization process, steps have been followed to functionalize MXene such that optimum concentrations of anti-CD63 and anti-E2F5 antibody is achieved. 30 µl of 25% APTES has been dropped into the chamber to ensure the bonding between the –OH group of MXene and NH_2 group of APTES which has been kept at 37°C for a time of 2 hours. Next, antibody immobilization has been realized by pipetting 30 µl of anti-CD63 and anti-E2F5 antibodies into the PDMS well followed by 30 µl of BSA to avoid nonspecific binding. For optimizing the parameters, incubation of antibodies has been performed at 37°C for a time of 1, 2 and 4 hours for different concentrations of 10, 20, 50, 70 and 100 µg/ml. Subsequently, FITC tagged secondary antibodies have been applied followed by washing to remove the unbound antibodies. Fluorescence microscopy has been performed to assess the efficacy of the primary antibody immobilization (details in **Supporting Information S4**). As control, FITC tagged antibodies have also been pipetted onto the sensors without any primary antibody. **Figure 4a** represents the variation of intensities for anti-E2F5 and anti-CD63 antibody binding with different incubation times at a fixed concentration of 100 µg/ml for sensor 2 fabricated with a GMX ratio of 1:1. For every incubation time, five sensors have been considered corresponding to each case. It has been observed that for all the times of incubation, the fluorescence intensity of the sensors with only BSA or in presence of only PBS is appreciably lower than that for the primary antibodies. Further, it has been indicated that the output saturates after 2 hours. Thus, subsequently, antibody binding intensities have been investigated for different sensors with varying antibody concentrations for an incubation time of 2 hours (**Figure 4b**). For every concentration, five sensors have been tested corresponding to each ratio and the resulting mean and standard deviations have been plotted in **Figure 4b**. It is observed that the output nearly saturates for a concentration of 60 µg/ml antibody concentration for all the sensors. Also, the antibody binding density is smaller in sensor 3 (1:3 GMX ratio) compared to that of sensors 2 (1:1 GMX ratio) and 1 (3:1 GMX ratio). This may be correlated with the specific surface area estimated from pore area analysis in Section 2.3. Further, the binding

enhancement of the antibodies at the optimized concentration and incubation time for the graphene-MXene transistor having 1:1 ratio (30 sensors considered for each antibody, taking 10 from each chip set) with respect to graphene FETs has been verified to be around 2.5 times across all the chip sets (**Figure 4c**). A representative fluorescence image aided with secondary antibody before and after E2F5 immobilization on sensor 2 with 1:1 GMX ratio has been represented in **Figure 4d** and **4e** respectively.

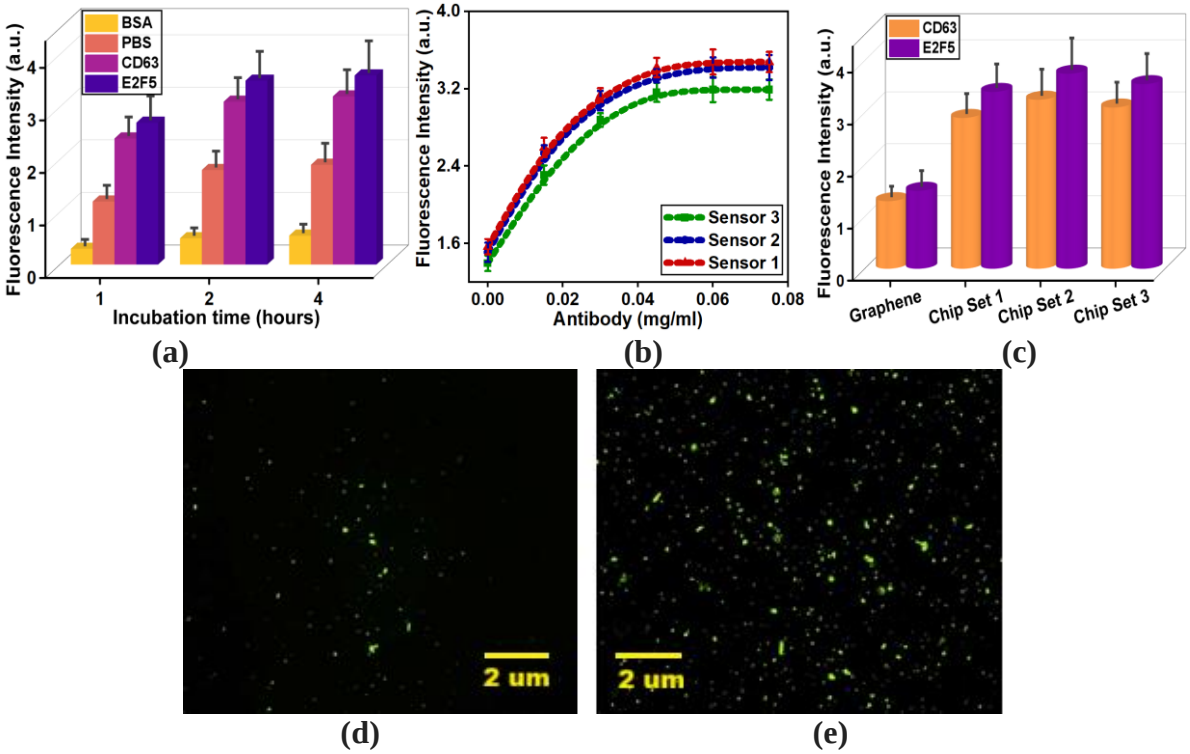

Figure 4. (a) Variation in fluorescence intensity corresponding to antibody binding as a function of incubation time at a fixed antibody concentration of 100 µg/ml for sensor 2 fabricated with GMX ratio of 1:1. Control experiments performed with BSA and PBS. (b) Antibody binding intensities measured after 2 h incubation for sensors fabricated with different GMX ratios as a function of antibody concentration. (c) Antibody binding enhancement of the antibodies for the graphene-MXene transistor (1:1 ratio) with respect to graphene FETs for three chip sets, taking 10 from each, representing the mean with its deviation. (d,e) Representative fluorescence microscopy images of the sensor surface (d) before and (e) after E2F5 immobilization.

2.5. Exosome pre-concentration under applied electric fields

In a fluidic environment, molecular capture can be facilitated by AC electric fields by various external forces such as DEP and ACEO. The AC electric field is applied across the gate and

shorted drain-source electrodes (so that no drain-source current flows through graphene) when the target analyte with the exosomes is dispensed onto the sensor surface. During this time, dc gate voltage is off, to avoid any shifting of operating point. In a liquid environment, the surface of the sensing material and the electrodes are surrounded by the electrical double layer of ions and the interaction between these ions and the tangential component of the external electric fields at these surfaces result in AC electroosmotic flows. On the other hand, the dielectrophoretic (DEP) force refers to the movement of polarizable particles in response to a non-uniform electric field, driven by the interaction between the induced dipole moments and the external fields. Depending on the particle's polarizability, it moves either toward regions of higher electric field (positive DEP or p-DEP) or lower electric field (negative DEP or n-DEP) to reach stable electrostatic potential energy states. Without the influence of these electric field-induced forces, exosome accumulation during the sensing process is mainly limited by diffusion-driven transport. For a solution with initial concentration, C_0 of target analyte, the time (t) required to accumulate n number of analytes by irreversible adsorption process on a circular disk-shaped electrode of radius a is theoretically given as $t(n) = \frac{n}{4DC_0a}$, where D represent the diffusion constant of analytes.[35] This expression indicates that for a single exosome to be adsorbed on an approximately 100 µm diameter, it will take several hours for a concentration level of 1000 particles ml^{-1}. A combination of DEP and ACEO can promote active transportation and concentration of the suspended nanoparticles to the sensing surface.

First, ACEO has been performed to drive the particles towards the sensor surface from the bulk liquid. In ACEO flow activated at low frequency, a time-averaged Maxwell force consistently directs flow from the electrode edges toward the channel surface, generating an electro-osmotic slip velocity, expressed by Helmholtz-Smoluchowski equation:

$$\langle u_s \rangle = \frac{-\epsilon_m}{4\eta} \Lambda \frac{\partial}{\partial x} |\phi - V|^2 \quad (2)$$

where, where Λ is the ratio between the potential drop over the diffuse part of the electrostatic double layer and the potential drop over the complete double layer, which was assumed to be 0.5,[36] ϕ is the potential located at the outer surface of the electrostatic double layer and V is the potential applied to the electrodes. ϵ_m and η are the permittivity and viscosity of the medium respectively. To perform the ACEO, a 2V peak-to-peak sinusoidal waveform with frequency sweep from 1 to100 kHz has been applied between the gate and the common drain-source electrodes. From the theoretical simulations using finite element tool of COMSOL Multiphysics 6.0 using simplified hemispherical constructs for the porous sensor morphology, it has been unravelled that ACEO drags the particles closer to the surface and generates a

surficial flow, concentrating the particles from the edge to edge to the centre of the sensing surface. However, for the selection of the optimum frequency, a combined ACEO and DEP simulation has been performed.

Dielectrophoretic force (DEP) which directs the motion of polarizable particles within a non-uniform electric field is estimated by **Equation 3**.

$$F_{dep} = 2\pi r_p^3 \varepsilon_0 real(\varepsilon_p^*) real\left(\frac{\varepsilon_p^* - \varepsilon_m^*}{\varepsilon_p^* + 2\varepsilon_m^*}\right) \nabla |E_{rms}|^2 \quad (3)$$

where, r_p is the radius of the spherical particle in the field, ε_0 is the vacuum permittivity, ε_m^* is the complex relative permittivity of the fluid, ε_p^* is the complex relative permittivity of the particle and E_{rms} is the root mean square of electric field. Since electric field has been computed in frequency domain, the complex permittivity can be expressed as **Equation 4**.[27]

$$\varepsilon^* = \varepsilon - \frac{i\sigma}{\omega} \quad (4)$$

where, ε is the permittivity, σ is the electrical conductivity and ω is the angular frequency of the electric field. It is evident that DEP force is a function of the radius and molecule property like dielectric constant and depending on the Clausius Mossotti factor ($real\left(\frac{\varepsilon_p^* - \varepsilon_m^*}{\varepsilon_p^* + 2\varepsilon_m^*}\right)$), the molecules experience either p-DEP or n-DEP. In the sensor structure, depicted schematically in **Figure 1b**, the channel area is smaller than the gate, thereby increasing the intensity of electric field on the surface of former which necessitates p-DEP based molecule concentration. The variation of electric field on the sensor surface has been verified from COMSOL simulation (**Supporting Figure S3**). A finite element simulation with a computationally efficient representation of the porous sensor surface has been executed to estimate the trapping efficiency of exosomes of diameter in the range of 30-180 nm with an input particle concentration of 200 particles/ml (details in **Supporting Information S5** and **Figure S4**). It has been revealed that DEP force is weak at 1 kHz and ACEO dominates in this regime. At 10 kHz, the DEP and ACEO forces are comparable and the particles are concentrated near the center. At 100 kHz, the DEP forces are stronger and the particles are driven towards the edges and at 1MHz, n-DEP occurs (**Figure 5a)**. Thus, 10 kHz has been selected for experimentation with plasma of normal, benign and high-grade PC patients. The particle collection efficiency without and with field as estimated from finite element simulation is represented in **Figure 5b** and **5c**. SEM images of exosomes extracted from BPH patients has been captured with and without DEP after E2F5 antibody immobilization on sensor with 1:1 GMX ratio, a representative image of a single view plane on the sensor surface has been depicted in **Figure 5(d,e)**. ImageJ software has therafter

been employed to quantify exosome capture from SEM images across ten different fields by counting individual vesicles under conditions of with and without DEP. For each condition, a total of 30 sensors for 1:1 GMX ratio, considering 10 from each chip set has been experimented and a comparative assessment of DEP-assisted exosome enrichment across sensors in different chip sets has been presented in **Figure 5f**.

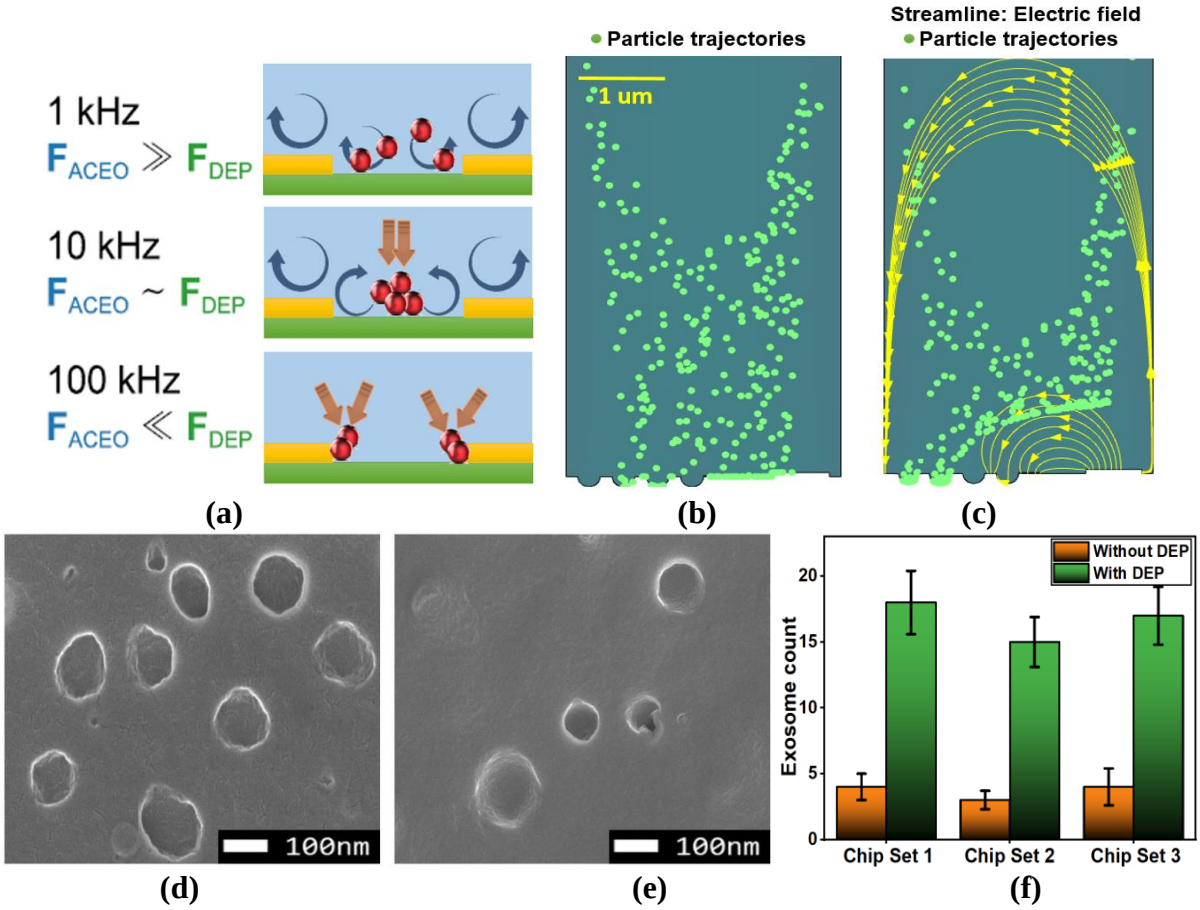

Figure 5. (a) Schematic illustration of the particle-trapping mechanism under applied AC electric fields at frequencies of 1 kHz, 10 kHz and 100 kHz. (b,c) Finite element simulation results depicting particle collection efficiency in the absence and presence of an applied electric field, respectively. (d,e) SEM micrographs of the sensor surface (GMX 1:1) following E2F5 antibody functionalization, acquired with and without/ dielectrophoresis. (f) Quantitative analysis of exosome density performed using ImageJ by counting individual vesicles from SEM images obtained under DEP-off and DEP-on conditions, enabling a comparative evaluation of DEP-assisted exosome enrichment across three chip sets (considering 10 from each).

2.6. Graphene-MXene transistor characterization

The sensing signal from a FET sensor is typically transduced from the surface potential into change in the channel conductance (*G*) upon adsorption of target analytes. The sensor response

for multiple dispersions of graphene connected in a combination of series-parallel configurations between a pair of source and drain electrodes can be described simplistically by **Equation 5**:

$$\frac{\Delta G}{G} = \frac{\sum_{j=1}^{C} \frac{\sum_{i=1}^{T} \frac{\Delta Q_{ij} kl_{ij}}{A_{ij} Q'_{ij} Q_{ij}}}{\sum_{i=1}^{T} \frac{kl_{ij}}{A_{ij} Q'_{ij}} \sum_{i=1}^{T} \frac{kl_{ij}}{A_{ij} Q_{ij}}}}{\sum_{j=1}^{C} \frac{1}{\sum_{i=1}^{T} \frac{kl_{ij}}{A_{ij} Q_{ij}}}} \quad (5)$$

where T and C represent the number of graphene-Mxene nanoflakes connected in serial and parallel configurations respectively, Q_{ij} , l_{ij} and A_{ij} are the effective associated charge, length and cross-sectional area of each nanoflakes respectively considering inhomogenity, Q_{ij}' represents the changed charge after biomolecule capture and ΔQ_{ij} indicates the change in effective charge for each nanoflakes.

The variation of drain-source current (I_{ds}) with gate-source voltage (V_{gs}) of graphene-MXene composite layer represented in **Figure 6a** (detailed method of electrical characterization in **Supporting Information S6**) indicates that the hole current decreases with increasing MXene concentration which may be attributed to n-doping of graphene by MXene. Excess amount of MXene may also cause enhanced Coulomb scattering. Though the specific surface area of sensor 1 and 2 are comparable, the size of the exosomes for BPH and PC patients being around 100 nm, the graphene-MXene composite with 1:1 ratio (sensor 2) has been selected for further sensing experiments. As the average pore size of sensor 1 is smaller than the mean diameter of exosomes, most exosomes are likely to be captured at the pore entrance rather than within the pores. Consequently, their surface charges are largely screened by the surrounding electric double layer of ions. In contrast, for sensor 2, whose average pore size slightly exceeds the exosome diameter, exosomes have a higher probability of entering the pores. This partial confinement limits complete electrostatic screening, as the finite Debye length leads to overlap of the ionic double layers, thereby enhancing charge sensitivity, as discussed in Section 2.1. The interfacial capacitance has been verified by cyclic voltammetry measurements which have been executed by connecting the drain and source electrodes to act as working electrode, the Ag/AgCl gate behaves as reference electrode and an additional gold electrode as counter. The scan has been performed for two different rates of 500 mV/sec and 100 mV/sec (details in **Supporting Information S7**). It is observed from **Figure 6b** that the current is reduced by 1.5 times in graphene-MXene substrate for any scan rate compared to only graphene which may be correlated to the decreased interfacial capacitance of the former with the electrolyte. As the dielectric constant and the active area are not expected to change significantly at the graphene-

MXene interface, the decreased current for graphene-MXene surface may be caused by the increased screening distance or effective Debye length. The measurements corresponding to each scan rate has been executed with five devices, for both the categories and the mean cyclic-voltammetry characteristics have been estimated. For each device, measurement has been performed till the consecutive curves overlap, which has then been recorded for further computation. The standard deviations for both the devices have been observed to be within 7%. Graphene-MXene thin film field effect transistor (categorized as two sets for the two antibodies) have been extensively characterized in presence of buffer (1 mM PBS, pH of 7.4) with gate connected to a dc voltage as represented in **Figure 6c**. In both the cases ambipolar characteristics have been observed where the conductance of the graphene-MXene channel has been modulated by the accumulated ions of the electrolyte through either p or n-type doping. As the transconductance is more for negative V_{gs}, it is implied that, graphene-MXene is predominantly p-type. In I_{ds}-V_{gs} characteristics, the variation of V_{ds} has resulted in deviation of Dirac point between V_{gs} of 0.2 and 0.4 V, which can be ascribed to the difference in work function difference between graphene and Ag/AgCl gate electrode. Each measurement has been performed on five sensors. All these measurements have been repeated with time till the transfer curves and hence the position of the Dirac point attains stability in presence of PBS.

To ensure device stability and measurement reproducibility during clinical testing, stringent exclusion criteria has been implemented based on the electrical characteristics of the remaining 810 fabricated FET devices from three printed circuit boards (**Figure 6d**). The devices exhibiting a Dirac voltage of V_D = 0.30 ± 0.15 V have been considered for further experimentation. Additionally, for stricter control of device reliability in batch scale fabrication, the possible adverse effects of leakage conduction through the electrodes and ions of the buffer (due to unwanted direct contact with the buffer in case of accidental non-uniformity in the graphene-MXene layer) have been reduced by patterning a PDMS well to cover the drain and source electrodes and engulf the gate electrode to provide sufficient volume for accommodating 100 µl of buffer/analyte (Device fabrication details in **Supporting Information S1**). Also the leakage current has been estimated to be approximately 50 nA which is almost 3 orders of magnitude lower than the lowest I_{ds}, thereby ensuring negligible interference in sensing. However, for sensing, the intrinsic device noise needs to be estimated since it affects the limit of detection. To facilitate the experimental noise measurement, I_{ds} corresponding to a V_{gs} of-0.5V has been recorded for both the antibodies in 1 mM PBS, before and after exposure to artificial plasma. These measurements have been recorded till the device characteristics stabilize in presence of buffer and plasma. **Figure 6e** represents the mean time dependent

current recordings for all the sensing devices considering the three chip sets before and after both the antibody immobilization, entirely in buffer. It has been observed that the fluctuations somewhat reduce post functionalization which may be attributed to the decrease in the exposed reactive groups of graphene-MXene surface. Similar experiments have been also conducted after exposing the sensor surface to artificial plasma for a duration of 10 minutes (which is the typical detection time) followed by washing and subsequent pipetting of PBS, as exhibited in **Figure 6f**. It is revealed that the fluctuations, increase which is inevitably caused by the presence of residual interfering molecules. The generation-recombination (G-R) of the electronic charge carrier caused by defects induced trapping and de-trapping at the channel-electrolyte interface along with charge fluctuations at the vicinity getting coupled through an effective gate capacitance lead to fluctuations in the current. This results in *1/f* noise behavior depicted by equation 6, which is also reflected in the noise spectra of **Figure 6g**.

$$S_I = N_A \frac{I_{ds}^2}{f^\beta} \tag{6}$$

where β usually deviates from 1 and N_A is a constant. It is reflected in **Figure 6g** that the noise magnitude correlates with the transient fluctuations. The lower noise magnitude, even in presence of plasma exposure is indicative of the superior quality of the devices. At this stage, the faulty devices have been isolated based on the Dirac point values and noise spectra, computed from the transient fluctuations. A total of 690 functional devices have been selected across all chip sets for further analysis.

The functional devices in each chip set has thereafter been divided into two sets A and B in an arbitary fashion for further testing with two different antibodies. Upon introducing anti-E2F5 (set A) and anti-CD63 (set B) antibodies, both the Dirac point shift and percentage change in I_{ds} have been recorded (**Figure 6(h,i)**). The fractional change in current ($\Delta I_{ds}/I_{ds}$) is expressed as percentage, at a V_{gs} of -0.5V, corresponding to maximum transconductance. (**Supporting Figure S5**). For every chip set, the deviation is within 5% which represents the intra-device reliability. Furthermore, the inter-chip statistical analysis confirms that the observed variations are not statistically significant (p: ns).

2.7. Sensing Framework for sEV Detection

Artificial plasma samples with negligible exosome concentrations, undergoing standard processing (details in **Supporting Information S8**) have been directly dispensed as 100 µl droplets without any dilution.

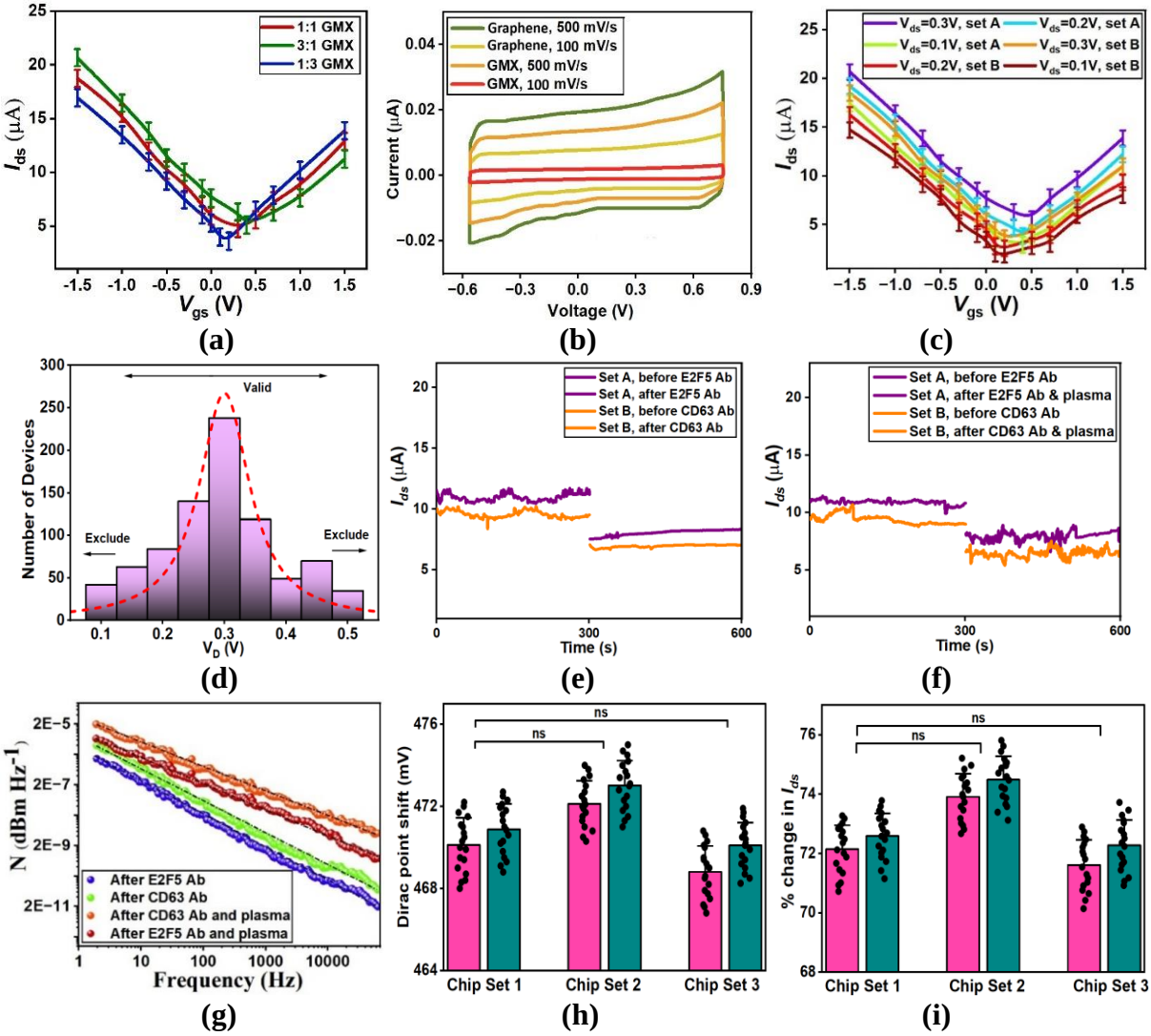

Figure 6. (a) Drain-source current (I_{ds}) as a function of gate-source voltage (V_{gs}) for FETs fabricated using different GMX ratios. (b) Cyclic voltammetry characteristics of both graphene (rGO) and GMX composites. (c) I_{ds}-V_{gs} characteristics recorded at varying V_{ds} in buffer conditions. (d) Statistical distribution of Dirac voltages obtained from around 810 fabricated FET devices, used to define exclusion criteria for ensuring device stability and measurement reliability. (e,f) Mean time-dependent current responses of the sensing devices recorded before and after antibody immobilization, measured (e) in buffer and (f) in plasma. (g) Mean noise power spectral density of the FET sensors, demonstrating stable electrical performance.(h,i) represent Dirac point shift and percentage change in I_{ds} respectively, measured upon immobilization of anti-E2F5 (Set A, pink color) and anti-CD63 (Set B, green color) antibodies.

The sEVs have been derived from grade GS7 prostate cancer patients (patient recruitment details in **Supporting Information S9**) by ultracentrifugation and then serially diluted to yield various concentration levels. The initial concentration has been estimated to be approximately

4.04 x 10^8 exosomes/ml (as indicated in **Figure 2d**). The Dirac point shifts for the two sets of devices at a particular V_{gs} has been estimated as a function of exosome concentration (**Figure 7(a,b)**). To clearly depict the device to device variation in Dirac points for the lowest exosome concentration of 200 particles ml^{-1}, **Figure 7c** and **7d** represent the deviations in the Dirac point measurements using both the antibodies in buffer and plasma, with and without electric field. For each concentration and condition in every set, 10 devices have been tested. The results indicate that both in buffer and plasma, anti-E2F5 antibodies exhibits slightly higher Dirac point shift than anti-CD63 antibodies which may be attributed to the upregulation of the former.[5-7] Further, application of AC electric field enables higher capture of exosomes within a time of 10 minutes, thereby generating greater sensor response. For sensors with anti-CD63 antibodies, the mean Dirac point exhibits left shifts by 14 mV and 37 mV while for anti-E2F5 antibodies, the shifts are 15 mV and 42 mV, without and with presence of ac electric field respectively for an exosome count of 200 particles ml^{-1} in buffer. This may be ascribed to the fact that without any electric field, lower numbers of exosomes are captured. In presence of DEP and ACEO aided capture, the increase in the shift of Dirac point may be contributed by higher capture of sEVs. The left shift of Dirac point upon capture of exosome for all the cases is indicative of negative surface charge of exosomes.[37] In presence of plasma, the mean Dirac point shift reduces to 12 mV without field and to 31 mV with electric field for anti-E2F5 antibodies, possibly due to the presence of non-specific proteins in the analyte. It becomes evident that for both the antibodies (**Figure 7c and 7d**), the Dirac point positions overlap significantly without electric field whereas, the application of electric field enables clear separation in Dirac point positions, with and without exosomes, in plasma.

Similar trend has been followed in the fractional change in I_{ds} ($\Delta I_{ds}/ I_{ds}$) (**Figure 7(e,f)**). The graphene-MXene FET sensor exhibits a detection limit of 200 exosomes/ml in plasma with both the antibodies in presence of field, since the percentage change in current (~35%) is almost three times the baseline current fluctuations(~12%). It has a wide range spanning six orders of magnitude, greater than 10^8 exosomes/ml and detection time of 25 minutes considering the field application time in plasma. The response with anti-E2F5 antibodies has been fitted by a linear regression curve having slope of 5.416 ± 0.25 and a R^2 value of 0.987.

Further, the typical selectivity of anti-E2F5 functionalized sensors in presence of electric field towards other biomolecules commonly present in plasma like IgG, lysine, PSA, HSA and inflammatory cytokine like IL-6 has been observed to be satisfactory (**Figure 7g**). Moving further, the device-to device variation in transient characteristics of I_{ds} before and after exposure to exosomes (200 particles ml^{-1}) in plasma with and without electric field have been represented

in **Figure 7(h,i)** for both the antibodies. It is observed that for both the antibodies (**Figure 7h and 7i**), in absence of AC electric field, there is a significant overlap in the I_{ds} measurement before and after exposure to exosomes with 200 particles/ml concentration. However, in presence of electric field, the sensor response is distinguishable across all devices tested. The subsequent section validates the clinical efficacy of the anti-E2F5 antibody functionalized sensors.

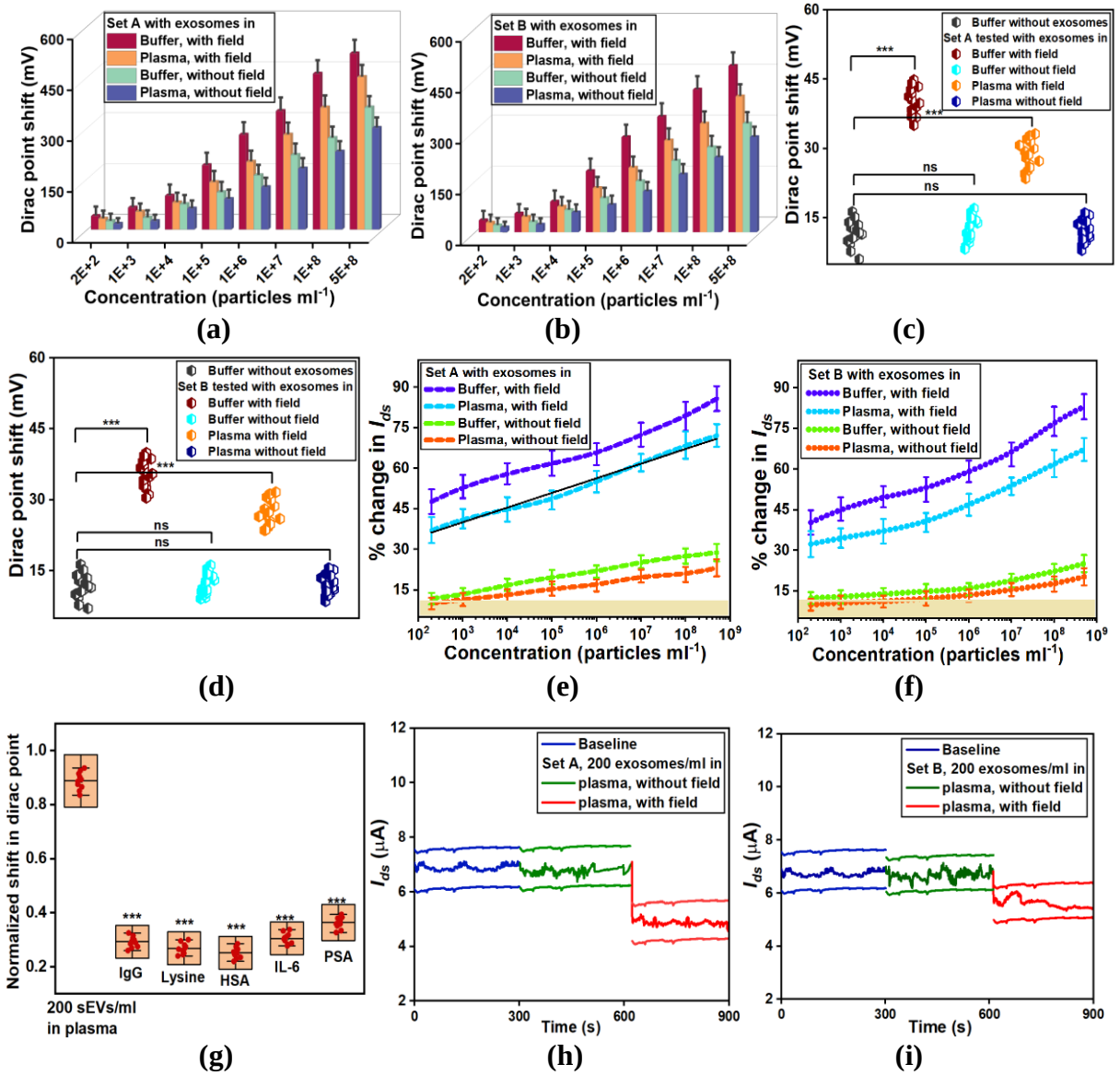

Figure 7. (a,b) Dirac point shifts with varying concentration under different conditions and (c,d) deviations in the Dirac points using both the antibodies in buffer and plasma in presence of 200 sEVs ml^{-1}, with and without electric field, (e,f) % change in current at a particular V_{gs} as a function of exosome concentration in both buffer and plasma; with and without the application of field, (g) Selectivity test in presence of electric field, with ***p < 0.001, (h,i) device-to device variation in transient characteristics of I_{ds} before and after exposure to 200 sEVs ml^{-1} in plasma with and without electric field for both the antibodies.

2.8. Clinical Performance of Exosomal E2F5 Based on Machine Learning Models

The clinical interpretation efficacy of both the antibody functionalized sensors have been initially evaluated with an unbiased, balanced and randomly allocated participant cohort which includes 150 BPH and PC patients besides 60 healthy individuals (HC). The cohort of patient samples has been obtained from SSKM Hospital (**Supporting Information S9**). This clinical study was approved by the institutional review board of IPGME&R and SSKM Hospital (IPGME&R/IEC/2022/480) and complied with the ethical principles outlined in the Declaration of Helsinki.

For this purpose, six more chip sets have been fabricated, immobilized with both the antibodies and electrically characterized, as discussed in Section 2.6 and the faulty devices have been isolated. Both the categories of sensors have been characterized with the plasma of the clinical samples without ultracentrifugation (**Supporting Figure S6**). The operational steps for extracting plasma from whole blood of patients has been outlined in **Supporting Information S8**. Although the overall sensor response amplitudes are comparable for both antibodies, anti-CD63 functionalized sensors exhibit substantial signal overlap between healthy and BPH cohorts, compared to anti-E2F5–functionalized sensors, underscoring the superior specificity of E2F5 as an exosomal biomarker for prostate cancer. However, the difference in exosome abundance between healthy and BPH cohorts is not sufficient and hence will limit the classification accuracy based solely on sensor response, even when probed with anti-E2F5 antibodies. To enable rigorous clinical validation, the diagnostic performance of the proposed sensing platform is therefore enhanced through artificial intelligence–driven data analysis. The decision tree ensemble classification framework, which is the random forest has been employed in this work to facilitate graded classification of PC patients owing to its robustness in handling small to moderate sized datasets, the model description of which has been detailed in the **Supporting Information S10**. The clinical classification model has been constructed during the training phase using random forest analysis and subsequently validated through cross-validation in the test phase, the schematic of which is depicted in **Figure 8a**. To additionally access multilevel classification outcome via the model's interpretive accuracy, random forest based regression has also been performed.

In order to verify the predictive ability of any classification/regression algorithms, broadening the dataset with the most relevant features from the sensor's response usually improves the accuracy.[38] Fractional change in I_{ds} and D_p are not the only parameters that shift upon the capture of exosomes. The shape of the I_{ds}-V_{gs} curves provides valuable information about the

analyte, as the slope varies. To enhance classification accuracy, we also extract the maximum and minimum transconductances (T_{max}, T_{min}), which correspond to the maximum change in hole and electron currents in response to the gate-to-source voltage, respectively. Hence to augment the discrimination between healthy, benign and different grades of prostate cancer patients, the response string encompasses extraction of four normalized parameters ($\Delta I_{ds}/I_{ds}$, ΔD_p, T_{max}, T_{min}) from steady-state transfer characteristics measurements. A feature ablation study has been performed which is a critical analytical technique used to evaluate the contribution and relevance of individual features in the predictive random forest model. It involves removing one or more features from the model and then assessing how this impacts the overall performance. The accuracy elucidating the ablation study of a single feature at a time has been illustrated in **Figure S7 of Supporting Information**, thus ensuring that the system relies on relevant, robust and meaningful features. It not only enhances model performance and stability but also strengthens its scientific credibility by confirming the importance of key features.

To assess the capability of E2F5 signature from the sensor's response for differentiating cancerous patients from healthy control, 40 PC out of a total of 150 PC samples (BPH+GS7+GS9) and 15 HC out of the entire available 60 HC samples has been randomly assigned to the training set, while the remaining samples have been used for testing the model. The model demonstrated appreciable training accuracy, correctly identifying 93.75% of all PC patients (103 out of 110 cases) and achieving a 100% accuracy rate for healthy controls (**Figure 8b**). The diagnostic reliability has been further highlighted by an area under the receiver operating characteristic curve (AUC) of 0.99 (**Figure 8c**), indicating near-perfect discrimination between PC patients and healthy individuals. Subsequently, we evaluated the sensor efficacy in similarly clustered patient samples using the same training framework described above. To determine the sensor's effectiveness in detecting early-stage prostate cancer, we tested it on a cohort of 45 test patients diagnosed with early stage (GS7) PC. The results demonstrated that the sensor effectively differentiated early-stage PC cases from healthy controls, achieving a distinctive diagnostic accuracy of 93.33% (**Figure 8d**). The area under the receiver operating characteristic curve (AUC) reached 0.99 (**Figure 8e**), indicating near-flawless diagnostic accuracy. These findings are particularly noteworthy given the higher likelihood of misdiagnosis in early-stage PC, highlighting the sensor's potential as a reliable tool for detecting PC at its initial stages. In parallel, the diagnostic value of E2F5 immobilized sensors to detect advanced stage prostate cancer (GS9) has been validated using a test cohort of 60 patient samples. The outcomes reveal that the sensor successfully distinguished advanced-stage PC cases from healthy controls (HCs) with remarkable accuracy, achieving a

distinguishing accuracy of 98.33% (**Figure 8f**). The area under the receiver operating characteristic curve (AUC) reached an outstanding value of 1 (**Figure 8g**), signifying close-to-ideal diagnostic precision. Most importantly, 45 benign tumour patient samples (BPH) have been validated with the E2F5 modified sensor's response. Interestingly, the model bespeaks an impressive accuracy of 91.11% distinguishing healthy control from benign ones (**Figure 8h**). Further, the model has reached a AUC value of 0.98 implying its fidelity (**Figure 8i**). Taken together, our findings strongly support the diagnostic potential of the E2F5 modified sensor's response aided with random forest based classification system for prostate cancer diagnosis. The system demonstrated high sensitivity and specificity, making it a reliable tool for accurately identifying PC. Notably, its effectiveness was particularly pronounced in early-stage patients, where diagnostic challenges and misdiagnoses are more common. Additionally, the system exhibits robust performance in detecting patient's benign tumours for whom diagnostic guidelines are less established. These results underscore the clinical values highlighting its potential for early detection, precise risk stratification, and improved diagnostic accuracy, which could significantly enhance PC screening protocols and patient outcomes.

The classification outcomes generated by applying this decision rule to all test samples have been compiled and presented in a confusion matrix (**Figure 8j**). This matrix provides a comprehensive summary of the model's performance, displaying the number of true positives (TP), true negatives (TN), false positives (FP), and false negatives (FN). By visualizing the model's predictions against the actual sample classifications, the confusion matrix offers valuable insights into the accuracy of the diagnostic system. For the test GS9 cancer patient samples, higher statistical difference has been exhibited compared to HC samples, indicating a marked elevation (**$p < 0.05$). There has also been a profound difference between the GS7 PCs when compared with HCs. This significant difference has been consistently observed across all grades of cancer, highlighting the statistical difference in distinguishing malignant from non-malignant cases. The results also suggest that the subtle difference in the BPH patients can also be well differentiated from the HCs (**Figure 8k**). **Figure 8g** depicts the plot between the predicted cancer grade from the sensor with the actual cancer grade estimated from tissue biopsy method. It has been observed from regression analysis that the results are strongly correlated with R^2 value of 0.98 and **$p < 0.001$, indicating that the sensors have been successfully validated with sufficient accuracy.

Table 1 presents a comparison between electrochemical and FET-based exosome detection strategies in terms of biorecognition elements, limit of detection (LOD), test matrices, and clinical applicability. Both antibodies and aptamers have been employed as biorecognition

elements for exosome sensing; however, their clinical relevance differs considerably. Aptamers offer high specificity and affinity, but the complexity of their design and optimization remains a major limitation for translating such sensing platforms from the laboratory to clinical use. In contrast, antibody-based systems, despite typically exhibiting higher LODs demonstrate stronger clinical applicability and compatibility with real biological samples. While most previous studies have focused on advanced cancer stages or conditions with distinct exosomal signatures, the present work addresses a far more nuanced diagnostic challenge: differentiating benign prostatic hyperplasia (BPH) from both healthy states and prostate cancer (PC). This capability represents a significant advancement, as conventional biomarkers such as prostate-specific antigen (PSA) often fail to distinguish between BPH and early-stage PC, leading to diagnostic ambiguity. Importantly, the proposed antibody-based sensing platform enables direct analysis of human plasma and achieves an impressive LOD of 200 exosomes/ml, approximately three orders of magnitude lower than the most sensitive antibody-based reports to date and comparable to aptamer based reports. Further, the recent patents and a company named ExoDX Prostate report non-invasive prostate cancer detection based on exosomal miRNA sensing or gene profiling strategies but they are capable of detecting patients with Gleason score above 6 and provide binary classification. Consequently, this study not only demonstrates clinically relevant, high-sensitivity detection but also introduces a new diagnostic paradigm capable of resolving subtle differences across prostate disease stages.

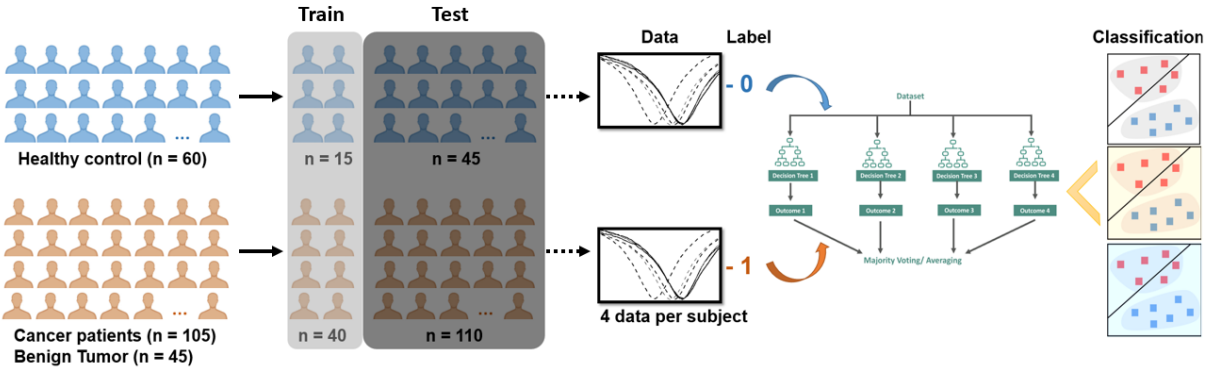

(a)

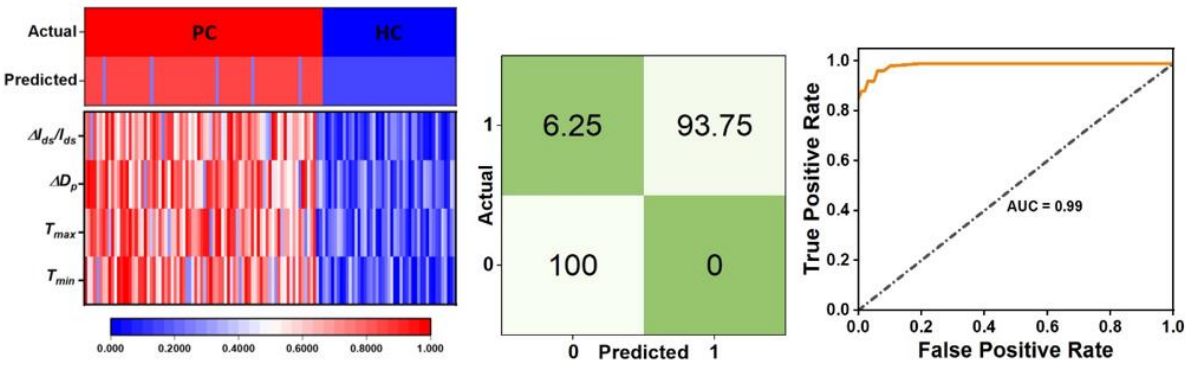

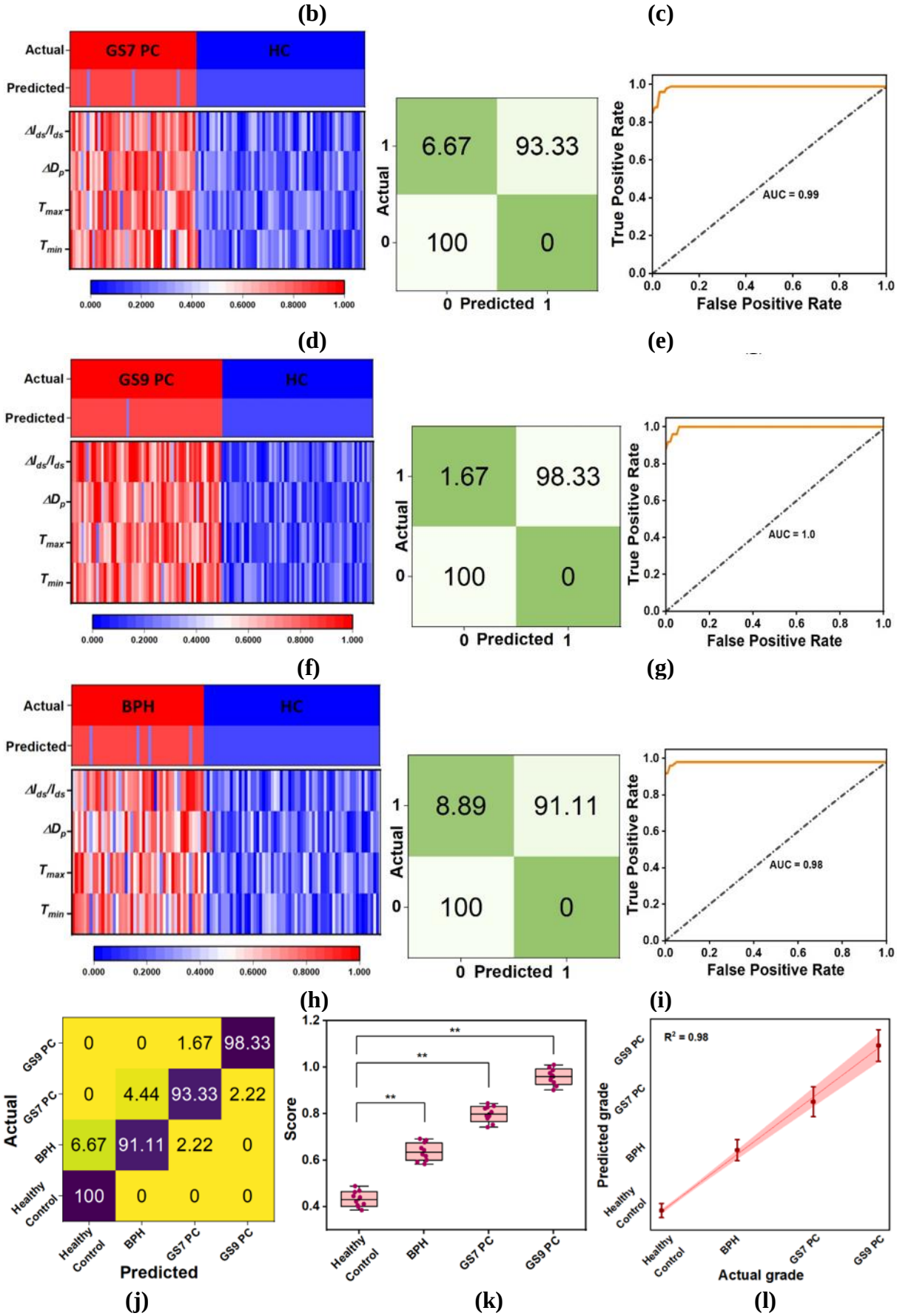

Figure 8. (a) Schematic of classification model, (b) Heat map showing the efficacy of E2F5 for discriminating between PC and HC samples (left), and a confusion matrix demonstrating the

predictive performance (right), (c) ROC analysis to evaluate the diagnostic efficiency of E2F5 for PCs and HCs, (d) Heat map for differentiating between early-stage PC and HC with its confusion matrix, (e) ROC analysis for early-stage PC with HCs, (f) Heat map for differentiating between advanced-stage PC and HC with its confusion matrix, (g) ROC analysis for advanced-stage PC with HCs, (h) Heat map for differentiating between benign tumor and HC with its confusion matrix, (i) ROC analysis for benign tumor with HCs, (j) Classification outcomes of all test samples, (k) Statistical analysis between cancer stages with HCs, (l) validation of the test dataset.

Table 1: Comparison table of electrochemical and FET based exosome detection strategies and their clinical applicability.

Ref. No.	Detection Principle, Bioreceptor	Target disease	LOD, Test analyte	Clinical Applicability
14	FET Antibody (anti-CD63, 7 anti-GPC-1)	Pancreatic Cancer	0.01 μg/μl (Blood plasma)	Detection of exosomes directly from clinical plasma samples, distinguishing different cancer stages
17	FET Aptamer (LZH8)	Hepatocellular carcinoma	242 particles/ml (Human serum)	Clinical detection in advanced stage HCC patients with respect to healthy controls
40	Electrochemical Aptamer (mApoc46 and CD63)	Ovarian Cancer	12 particles/μl (Human plasma)	Detection of exosomes directly from patient plasma diagnosed with HGSOC or non-HGSOC, discriminates between HGSOC patient stages
39	FET Antibody (anti-CD63)	Prostate Cancer	33 particles/μl (Blood Serum)	Detection of exosomes from serum samples of advanced stage cancer patients and healthy controls
41	Electrochemical Aptamer (EpCAM)	Hepatocellular carcinoma	251 particles/ml (Blood serum)	Clinical detection in advanced stage cancer patients with respect to healthy controls
42	Electrochemical Aptamer (MUC1 and CD63)	Breast Cancer	3.0×10^4 Particles/ml (Human serum)	Detection of exosomes from serum samples of advanced stage cancer patients and healthy controls
43	Electrochemiluminescence Antibody (anti-CD63 and anti-CD9)	Pancreatic Cancer	400 particles/ml (Human serum)	Clinical detection of pancreatic cancer patients with respect to healthy controls

44	Electrochemiluminescence Aptamer (Au@luminol-PDL1 and Au@g-C3N4-MUC1)	Breast Cancer	1.62 x 10^3 exosomes/ml (Human serum)	Clinical detection of breast cancer patients with distinction from other cancer patients and with respect to healthy controls
	This work Antibody (anti-CD63, E2F5)	Prostate cancer	200 exosomes/ml (Human plasma)	Detection of exosomes directly from clinical plasma samples, Distinguishing different cancer stages: benign prostatic hyperplasia (BPH), early and advanced prostate cancer (PC), and healthy individuals

3. Conclusion

To summarize, herein, we develop an efficient electrochemical transistor platform based on graphene-MXene composite coupled with dielectrophoretic concentration of sEV. This platform offers three key features for the quantification of exosomes, which are vital for early prostate cancer (PC) diagnosis. Firstly, the porous structure of the composite mitigates the Debye screening effect by preventing the formation of a complete ion shielding layer. Further, DEP enrichment enhances the sensitivity of detection. Secondly, E2F5, a protein recently identified as upregulated in prostate cancer patients, has been validated for early detection of prostate cancer, with performance comparisons made to CD63 antibodies. Thirdly, various features such as changes in the drain-source channel current, Dirac point shifts, and transconductance extremes have been analyzed using machine learning-based classification methods. These analyses allow for differentiation between benign conditions and various grades of malignant tumors, aiding in prostate cancer diagnosis. The proposed sensing platform holds significant potential for advancing the application of electrochemical transistors in clinical settings, subjected to additional validation with larger patient cohorts.

Supporting Information

Supporting Information is available from the Wiley Online Library or from the author.

Acknowledgements

P. Mukherjee is grateful to MHRD, Govt. of India for the financial support for conducting the present research work. The study was supported by the funding from ANRF-PAIR, New Delhi (ANRF/PAIR/2025/000021/PAIR) received by C. RoyChaudhuri and Indian Council of Medical Research, New Delhi, (Project Reference No: 55/5/2012- BMS (Part V)) received by S. Sengupta. N. Sultana's predoctoral fellowship is supported by CSIR {09/0028 (13755/2022-EMR-1)}. We are grateful to all the study participants for their cooperation. S. Sengupta and N. Sultana thank Dr. Noushim Huda of Department of Urology, IPGMER & SSKM Hospital, Kolkata for his help in patient recruitment and are also thankful to Department of Biochemistry, University of Calcutta, for providing instrument facilities and infrastructure support. Authors also acknowledge Central Characterization Department of CSIR-IMMT for the characterization facilities. P. Mukherjee and N. Sultana contributed equally to this work.

References

[1] H. Sung, J. Ferlay, R. L. Siegel, M. Laversanne, I. Soerjomataram, A. Jemal, F. Bray, *CA Cancer J Clin*. **2021**, *71*, 209-249. https://doi.org/10.3322/caac.21660.

[2] M. R. Cooperberg, J. M. Broering, P. R. Carroll, *J Natl Cancer Inst.* **2009**, *101*, 878-87. https://doi.org/10.1093/jnci/djp122.

[3] A. Glaser, Z. Shi, J. Wei, N. A. Lanman, S. Ladson-Gary, R. E. Vickman, O. E. Franco, S. E. Crawford, S. L. Zheng, S. W. Hayward, W. B. Isaacs, B. T. Helfand, J. Xu, *Eur Urol Open Sci.* **2022**, *43*, 54-61. https://doi.org/10.1016/j.euros.2022.07.004.

[4] S. Majumder, A. Bhowal, S. Basu, P. Mukherjee, U. Chatterji, S. Sengupta, *J Cell Physiol.* **2016**, *231*, 2482-92. https://doi.org/10.1002/jcp.25361.

[5] D. Karmakar, J. Maity, P. Mondal, P. S. Chowdhury, N. Sikdar, P. Karmakar, C. Das, S. Sengupta, *Carcinogenesis.* **2020**, *41*, 1767-1780. https://doi.org/10.1093/carcin/bgaa043.

[6] D. Karmakar, P. Lahiri, M. Bedi, A. Ghosh, A. Ghosh, A. Barui, S. K. Varshney, B. Lahiri, S. Sengupta, *J Cell Biochem.* **2023**, *124*, 849-860. https://doi.org/10.1002/jcb.30408.

[7] N. A. Huda, S. Chatterjee, N. Sultana, S. Sengupta, D. Sarkar, *Urologia.* **2025**, *5*, 3915603241313276. https://doi.org/10.1177/03915603241313276.

[8] P. Mukherjee, S. Dasgupta, A. Barui, C. RoyChaudhuri, *ACS Appl. Electron. Mater.* **2025**, *7*, 2313–2326. https://doi.org/10.1021/acsaelm.4c02084.

[9] M. Tian, J. Wei, E. Lv, C. Li, G. Liu, Y. Sun, W. Yang, Q. Wang, C. Shen, C. Zhang, B. Man, J. Wang, B. Zhao, S. Xu, *Chemical Engineering Journal* **2024**, *498*, 155355. https://doi.org/10.1016/j.cej.2024.155355.

[10] H. Cui, T. Zheng, N. Qian, X. Fu, A. Li, S. Xing, X. F. Wang, *Small* **2024**, *20*, 2402434. https://doi.org/10.1002/smll.202402434.

[11] P. Li, J. Chen, Y. Chen, S. Song, X. Huang, Y. Yang, Y. Li, Y. Tong, Y. Xie, J. Li, S. Li, J. Wang, K. Qian, C. Wang, L. Du, *Small* **2023,** *19*, 2207381. https://doi.org/10.1002/smll.202207381.

[12] Ö. Altıntaş, Y. Saylan, *Anal. Chem.* **2023**, *95*, 16029–16048, https://doi.org/10.1021/acs.analchem.3c02224.

[13] Z. Liu, B. Pang, Y. Wang, J. Zheng, Y. Li, J. Jiang, *Small.* **2025**, *21*, 2405872, https://doi.org/10.1002/smll.202405872.

[14] T. Yin, L. Xu, B. Gil, N. Merali, M. S. Sokolikova, D. C. A. Gaboriau, D. S. K. Liu, A. N. M. Muhammad, S. Alodan, M. Chen, O. Txoperena, M. Arrastua, J. M. Gomez, N. Ontoso, M. Elicegui, E. Torres, D. Li, C. Mattevi, A. E. Frampton, L. R. Jiao, S. Ramadan, N. Klein, *ACS Nano*. **2023**, *17*, 14619-14631. https://doi.org/10.1021/acsnano.3c01812.

[15] S. Ramadan, R. Lobo, Y. Zhang, L. Xu, O. Shaforost, D. K. H. Tsang, J. Feng, T. Yin, M. Qiao, A. Rajeshirke, L. R. Jiao, P. K. Petrov, I. E. Dunlop, M. M. Titirici, N. Klein, *ACS Appl Mater Interfaces.* **2021,** *13*, 7854-7864. https://doi.org/10.1021/acsami.0c18293.

[16] J. An, H. Park, J. Kim, H. Park, T. H. Kim, C. Park, J. Kim, M. H. Lee, T. Lee, *ACS Sens.* **2023**, *8*, 3174-3186. https://doi.org/10.1021/acssensors.3c00879.

[17] Y. Chen, D. Kong, L. Qiu, Y. Wu, C. Dai, S. Luo, Z. Huang, Q. Lin, H. Chen, S. Xie, L. Geng, J. Zhao, W. Tan, Y. Liu, D. Wei, *Anal Chem.* **2023**, *95*, 1446-1453. https://doi.org/10.1021/acs.analchem.2c04433.

[18] G. S. Kulkarni, Z. Zhong, *Nano Lett.* **2012**, 12, 2, 719-723. https://doi.org/10.1021/nl203666a.

[19] P. Mukherjee, P. Dutta, K. Sinha, S. Sen, T. Shirke, R. Ganguly, A. Barui, C. RoyChaudhuri, *Appl. Phys. Lett*. **2023**, 123, 193701. https://doi.org/10.1063/5.0168729.

[20] H. Alvandi, F. Asadi, A. H. Rezayan, H. Hajghassem, F. Rahimi, *Anal Chim Acta.* **2025**, *1348*, 343816. https://doi.org/10.1016/j.aca.2025.343816.

[21] V.N. S. Kumaran, M. Venkatesh, A. S. Alqahtani, A. Mubarakali, P. Parthasarathy, *Materials Science in Semiconductor Processing* **2025**, 186, 109071. https://doi.org/10.1016/j.mssp.2024.109071

[22] X. Guan, J. Zhao, Z. Sha, Y. Liang, J. Huang, J. Zhang, S, Sun, *Biosens. Bioelectron.* **2024**, *259*, 116380. https://doi.org/10.1016/j.bios.2024.116380.

[23] D. G. Mathew, P. Beekman, S. G. Lemay, H. Zuilhof, S. Le Gac, W. G. van der Wiel, *Nano Lett.* **2020**, *20*, 820-828. https://doi.org/10.1021/acs.nanolett.9b02741.

[24] H. Yoo, H. Jo, S. S. Oh, *Mater. Adv.* **2020**, *1*, 2663-2687. https://doi.org/10.1039/D0MA00639D.

[25] D. Zhou, Y. Cui, P.-W. Xiao, M.-Y. Jiang, B.-H. Han, Nat Commun **2014**, 5, 4716. https://doi.org/10.1038/ncomms5716

[26] S. Khatun, S. Samanta, S. Sahoo, I. Mukherjee, S. Maity, A. Pradhan, *Chemistry A European Journal* **2024**, 30(68), e202403386. https://doi.org/10.1002/chem.202403386.

[27] Y. Zhang, Q. Wan, N. Yang, *Small* **2019**, 15(48), 1903780. https://doi.org/10.1002/smll.201903780.

[28] P. Rajput, S. Chatterjee, R. K. Sinha, P. Devi, *Microchim Acta* **2025**,*192*, 209. https://doi.org/10.1007/s00604-025-07067-3.

[29] S. Patra, N. U. Kiran, P. Mane, B. Chakraborty, L. Besra, S. Chatterjee, S. Chatterjee, *Surfaces and Interfaces* **2023**, *39,* 102969. https://doi.org/10.1016/j.surfin.2023.102969.

[30] L. Wang, G. He, W. Wang, X. Xu, S. Jiang, E. Fortunato, R. Martins, *Journal of Materials Science & Technology* **2023,** 159, 41-51. https://doi.org/10.1016/j.jmst.2023.02.046

[31] Y. Li, Z. Peng, N. J. Holl, M. R. Hassan, J. M. Pappas, C. Wei, O. H. Izadi, Y. Wang, X. Dong, C. Wang, Y. W. Huang, D. Kim D, C. Wu, *ACS Omega.* **2021**, *6*, 6643-6653. https://doi: 10.1021/acsomega.0c05421.

[32] L. Wang, G. He, W. Wang, X. Xu, S. Jiang, E. Fortunato, R. Martins, *Journal of Materials Science & Technology* **2023**, *159*, 41-51. https://doi.org/10.1016/j.jmst.2023.02.046.

[33] Shoorideh, K., Chui, C. O. On the origin of enhanced sensitivity in nanoscale FET-based biosensors. Proc Natl Acad Sci. **2014**, 111(14), 5111-5116.

[34] F. Liu, A. Zhou, J. Chen, H. Zhang, J. Cao, L. Wang, Q. Hu, *Adsorption* **2016**, *22*, 915-922. https://doi.org/10.1007/s10450-016-9795-8.

[35] E. S. Yu, E. T. Jeong, S. Lee, I. S. Kim, S. Chung, S. Han, I. Choi, Y. S. Ryu, *ACS Nano.* **2023**, *17*, 2114-2123. doi: 10.1021/acsnano.2c07933.

[36] H. T. M. Wiegerinck, J. A. Wood, J. C. T. Eijkel, R. G. H. Lammertink, I. Frankel, A. Ramos, *Langmuir* **2024**, *40*, 19988-19996, https://doi.org/10.1021/acs.langmuir.4c02135.

[37] D. K. H. Tsang, T. J. Lieberthal, C. Watts, I. E. Dunlop, S. Ramadan, A. E. del Rio Hernandez, N. Klein, *Sci Rep.* **2019**, *9*, 13946. https://doi.org/10.1038/s41598-019-50412-9.

[38] P. Mukherjee, S. Sen, A. Das, S. Kundu, C. RoyChaudhuri, *Biosens Bioelectron.* **2025**, *271*, 117023. https://doi.org/10.1016/j.bios.2024.117023.

[39] Y. Yu, Y. T. Li, D. Jin, F. Yang, D. Wu, M. M. Xiao, Zhang, H., Zhang, Z. Y., Zhang, G. J., *Anal Chem*. **2019**, 91(16), 10679-10686. https://doi.org/10.1021/acs.analchem.9b01950.

[40] F. Ge, W. Ding, C. Han, L. Zhang, Q. Liu, J. Zhao, Z. Luo, C. Jia, P. Qu, L. Zhang, *ACS Sens*. **2024**, 9(6), 2897-2906. https://doi.org/10.1021/acssensors.3c02776

[41] Ma Y, He XL, Du JQ, et al. Multistage Cascade-Hierarchical Nucleic Acid Amplification for Label-Free Ultrasensitive Electrochemical Sensing of Tumor-Associated Extracellular Vesicles. Anal Chem. **2026,** 98(3), 2214-2224. https://doi.org/10.1021/acs.analchem.5c06009

[42] L. Yang, X. Yin, B. An, F. Li, *Anal. Chem.* **2021**, 93, 1709-1716. https://doi.org/10.1021/acs.analchem.0c04308

[43] H. Xiong, Z. Huang, Q. Lin, B. Yang, F. Yan, B. Liu, H. Chen, J. Kong, *J. Anal. Chem.* **2022**, 94, 837−846. https://doi.org/10.1021/acs.analchem.1c03535

[44] K. Luo, Z. Jiang, L. Li, L. Lin, T. Qin, J. Li, *ACS Sens*. **2025**, 10, 5528−5538. https://doi.org/10.1021/acssensors.4c03666.